TECHNICAL MEMORANDUM

712

Air-Sea Interaction and Surface Waves

Peter A.E.M. Janssen, Øyvind Breivik, Kristian Mogensen, Frédéric Vitart, Magdalena Balmaseda, Jean-Raymond Bidlot, Sarah Keeley, Martin Leutbecher, Linus Magnusson, and Franco Molteni.

Research Department

November 2013

European Centre for Medium-Range Weather Forecasts
Europäisches Zentrum für mittelfristige Wettervorhersage
Centre européen pour les prévisions météorologiques à moyen terme

Series: ECMWF Technical Memoranda

A full list of ECMWF Publications can be found on our web site under:
http://www.ecmwf.int/publications/

Contact: library@ecmwf.int

European Centre for Medium-Range Weather Forecasts
Shinfield Park, Reading, RG2 9AX, England

1 Introduction

Presently we are developing a coupled earth system model that allows for efficient, sequential interaction of the ocean/sea-ice, atmosphere and ocean waves components, and, therefore it becomes feasible to introduce sea state effects on the upper ocean mixing and dynamics (Mogensen *et al.*, 2012). By the end of 2013, a first version of this system will be introduced in operations in the medium-range/monthly ensemble forecasting system. The main purpose of this operational change is that coupling between atmosphere and ocean is switched on from initial time, rather than from day 9-10 in the forecast. This version will also include a number of changes to the air-sea interaction that explicitly use information on the sea state from the wave model. These changes will be described in this report. In the mean time, work is in progress to introduce the sea-ice component in the forecasting and assimilation system while also a considerable amount of effort is devoted to the development of a weakly coupled data assimilation system. A first prototype of such a weakly coupled system is near completion and will be thoroughly tested in the context of the reanalysis effort.

Ocean waves represent the interface between the ocean and the atmosphere, the two most important systems governing the dynamics of weather, climate and global change. A realistic description of the physical processes occurring at the ocean-atmosphere interface is essential for a reliable determination of the air-sea fluxes of momentum, sensible and latent heat, CO_2 and other trace gases, and aerosols. It is known that the wave field is intimately involved in these exchange processes, and, therefore, wave models are needed to compute not only the wave spectrum, but also the processes at the air-sea interface that govern the fluxes across the interface.

In the context of these ideas, a wave prediction system, called the WAM model, was developed that determines the sea state dependence of the air-sea fluxes (Komen et al, 1994). As a first step, the study of the two-way interaction between ocean waves and atmospheric circulation was undertaken. This interaction takes place on a relatively short time scale of a few days. Modest improvements in medium-range forecasting of waves and winds were obtained (Janssen *et al.*, 2002; Janssen, 2004)) and, as a consequence, since the 29th of June 1998 ECMWF has been producing weather and ocean wave analyses and forecasts, using a coupled atmosphere, ocean-wave forecasting system. On a seasonal time scale, depending on spatial resolution, however, a more substantial impact of ocean waves on the atmospheric climate was found (Janssen and Viterbo, 1996). The next step in the development of one model for ocean and atmosphere is to study the impact of the sea state on the ocean circulation. These studies are only beginning and therefore we are, in this respect, still in an exploration phase. Nevertheless, already some promising developments may be reported.

In this paper we start with a discussion of the details of air-sea interaction, assuming that ocean waves play an important role in this interaction. Growing ocean waves play a role in the air-sea momentum and heat transfer while breaking ocean waves affect the upper ocean mixing. If the ocean model is regarded as a system that describes the evolution of the ocean circulation velocity then it will be found that there is, because of the presence of ocean waves, an additional force on the mean circulation, which is called the Stokes-Coriolis force. Furthermore, the surface stress felt by the mean circulation is the total surface stress applied by the atmosphere minus the net stress going into the waves. Finally, momentum transfer and the sea state are affected by surface currents, hence it makes sense to introduce a three-way coupling between atmosphere, ocean circulation/sea-ice and surface waves.

The programme of this paper is as follows. In §2 we briefly describe the most salient features of the role of ocean waves in air-sea interaction. Next, we indicate how sea state effects may be incorporated into large scale ocean circulation system. For reasons of economy compromises have to be made in the representation of processes such as wave-induced upper ocean mixing and the Stokes-Coriolis force. In

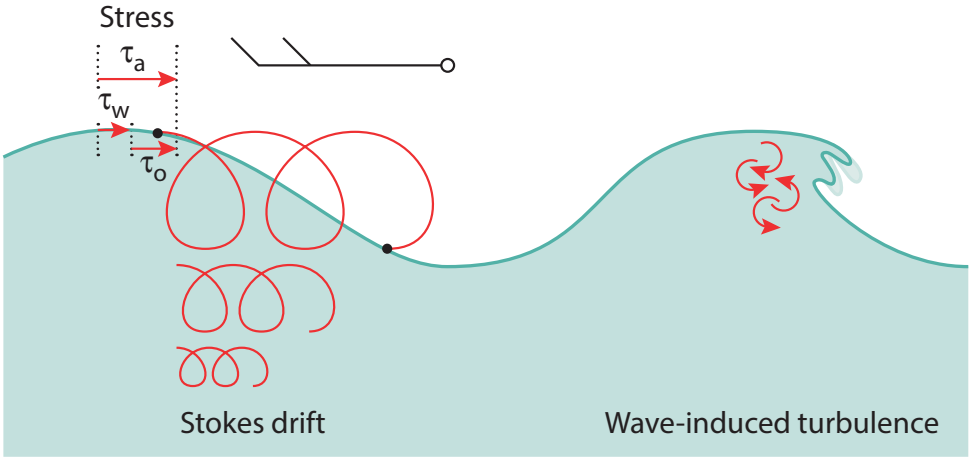

Figure 1: Wave-ocean interaction. As waves grow under the influence of the wind (left), the waves will absorb momentum which otherwise would have gone into the ocean directly. As waves break, turbulent kinetic energy is injected into the ocean mixed layer, significantly enhancing the mixing. The Stokes drift, caused by finite amplitude waves, sets up a current in the along-wave direction which decays rapidly with depth. Near the surface it may become substantial ($\simeq$ 1 m/s). The Coriolis effect works on the Stokes drift and adds a new term to the momentum equations known as the Stokes-Coriolis force.

§3 we present results of simulations with the NEMO model, which has been modified to include sea state effects on surface forcing, upper ocean mixing and including the additional Stokes-Coriolis force. Using in-situ observations we study the quality of the resulting SST fields by inspecting maps of systematic error and the standard deviation of error. The default of version 3.4 of NEMO includes sea state effects, but as there is no knowledge on the actual sea state it is assumed that the sea state is in equilibrium with the wind (in the field of ocean waves this is called 'old' windsea) and the energy flux due to breaking waves is a simple function of the friction velocity. Results with this version of NEMO are referred to as the control (CTRL). We assess the impact of sea state effects on the twenty year climate of the ocean circulation by comparing with CTRL, and typically differences of $\pm$ 1.5-2 $^{\circ}$K in SST have been found, which are fairly substantial. We also try to assess whether these differences at the surface result in changes to the deep circulation. After studying results with NEMO in forced mode, we continue in §4 with presenting results from fully coupled integrations on the seasonal timescale, where we concentrate on aspects of model drift and possible impact on predictability.

In the present operational medium-range/monthly ensemble forecasting system (ENS) the ocean becomes dynamically active from day 10 and onwards. First results using the new version of NEMO from day 0 in the ensemble prediction system and in the monthly system are presented in §5. Coupling from day 0 results in substantial improvements in probablistic skill of ENS and in predicting the MJO. Finally, it is well-known that during the generation of hurricanes there is a strong interaction between ocean and atmosphere. ENS was run for a number of special cases, and, in particular for slowly moving hurricanes a beneficial impact on the deepening of a low is found.

A summary of conclusions will be presented in §6.

2 Sea state effects

Over the past 40 years a considerable amount of research has been devoted to investigate the role of ocean waves in air-sea interaction. Important contributions to be mentioned are the pioneering work of Hasselmann (1971) on what is nowadays called the Stokes-Coriolis force, the thought-provoking work of McWilliams and Restrepo (1999) on the wave-driven ocean circulation and the courageous efforts by Craig and Banner (1994) on upper ocean mixing by wave breaking. In this Section we briefly discuss a number of sea state related processes that are thought to be important in the interaction between ocean and atmosphere. A pictorial view of the relevant processes is shown in Fig. 1.

Before we discuss some of the mathematical details of the processes involved it is important to realize that ocean waves give rise to transport of momentum. Therefore one needs to separate the contribution of the ocean waves from the total transport as an ocean model gives the evolution of the ocean circulation only. As a consequence, in a rotating ocean the ocean waves exert a wave-induced stress on the mean ocean circulation which results in a force equal to $\mathbf{u}_s \times \mathbf{f}$, where $\mathbf{f}$ is the Coriolis parameter, and $\mathbf{u}_s$ equals the Stokes drift. This additional force may have impact on the Ekman turning of the surface current. Secondly, the surface stress felt by the ocean circulation is the atmospheric stress minus the net stress going into the waves. Therefore, when waves are growing, momentum and energy is spent in growth which is not available for forcing the mean circulation while in the opposite case of a decaying sea state more momentum is available for forcing the ocean. Only when the sea state is in equilibrium the ocean is forced by the atmospheric stress, but in practice an equilibrium sea state is a fairly rare event. We will refer to this as sea-state dependent forcing.

Thirdly, starting with the work of Craig and Banner (1994) it is well-known that breaking ocean waves affect mixing of ocean current and temperature by enhancing turbulence in the upper ocean. The energy flux by surface wave breaking affects the upper-ocean mixing up to a depth of the order of the wave height. Transport to the deeper layers of the ocean is possible because work against the shear in the Stokes drift generates Langmuir cells and wave-induced turbulence which have a penetration depth of the order of the typical wavelength of the wave field (see e.g. Grant and Belcher, 2009).

In the following §'s some of the mathematical details of the sea state dependent processes will be given. For example, we have to give a clear distiction between wave momentum and momentum for the ocean circulation and we have to work out the consequences of this separation for the momentum budget of the ocean. This separation has consequences for how the ocean is being forced and it introduces the Stokes-Coriolis force. We also have to explain how effects of breaking ocean waves are introduced in upper-ocean mixing. A brief summary of this development is offered in §2.3.

2.1 Conservation of total mass and momentum

In order to understand better why one needs to include the Stokes-Coriolis forcing and why the mean ocean circulation is forced by the sea-state dependent stress, we need to study the conservation laws for total column mass and momentum in the presence of ocean waves. For a similar discussion see Janssen (2004).

Consider an incompressible fluid (water) in a constant gravitational field on a rotating earth. Let the body of water with air above it be of infinite extent in the horizontal while in the vertical it extends from $z = -D$ (with D the water depth) to $z = \eta$, with $\eta(x,y,t)$ the unknown surface elevation. Let us assume

that the water motion is governed by the continuity equation

$$\frac{\partial}{\partial t}\rho + \nabla \cdot (\rho \mathbf{u}) = 0. \tag{1}$$

and the momentum equation

$$\frac{\partial}{\partial t}\rho \mathbf{u} + \nabla \cdot \rho \mathbf{u}\mathbf{u} = -\nabla p + \rho \mathbf{g} + \rho \mathbf{u} \times \mathbf{f}. \tag{2}$$

These equations apply to the domain $-D < z < \eta$ and the boundary conditions are

$$z = \eta(x,y,t): \ \frac{\partial}{\partial t}\eta + \mathbf{u} \cdot \nabla_h \eta = w, \ p = p_a, \tag{3}$$

where p_a is the given air pressure at the sea surface and $\nabla_h = (\partial/\partial x, \partial/\partial y)$ is the horizontal gradient operator. At the flat bottom $D = D_0$ we impose the condition that no fluid penetrates the bottom

$$z = -D: \ w = 0. \tag{4}$$

Following Longuet-Higgins and Stewart (1961), Whitham (1962), and Phillips (1977) conservation laws for the mean surface elevation ζ and the mean horizontal velocity $\mathbf{U}$ may now be obtained by integration of the continuity equation and the momentum equation over the depth of the water, followed by a suitable ensemble averaging. The ensemble average $\langle . \rangle$ is supposed to filter the linear gravity wave motion. Here, the mean surface elevation ζ is defined as

$$\zeta = \langle \eta \rangle, \tag{5}$$

while the mean horizontal velocity $\mathbf{U}$ follows from

$$\mathbf{U} = \frac{\mathbf{P}}{\rho h}, \tag{6}$$

with $h = D + \zeta$ the slowly varying water depth. Note that $\mathbf{P}$ is the *total* mass flux

$$\mathbf{P} = \langle \int_{-D}^{\eta} dz \, \rho \mathbf{u} \rangle, \tag{7}$$

i.e., it consists of the sum of the water column mean $\mathbf{P}^m$ and the surface layer mean $\mathbf{P}^w$, defined as (Hasselmann, 1971)

$$\mathbf{P}^m = \langle \int_{-D}^{\zeta} dz \, \rho \mathbf{u} \rangle, \ \ \mathbf{P}^w = \langle \int_{\zeta}^{\eta} dz \, \rho \mathbf{u} \rangle. \tag{8}$$

In the linear approximation the surface layer mean mass flux may be expressed in terms of the wave momentum

$$\mathbf{P}^w = \rho g \int d\mathbf{k} \, \mathbf{l} \, F/c, \tag{9}$$

where c is the phase speed of the gravity waves and $\mathbf{l} = \mathbf{k}/k$ is a unit vector pointing in the direction of the wave propagation. As a consequence, the mean horizontal velocity $\mathbf{U}$ is the sum of the ocean circulation velocity $\mathbf{U}_c$ and the wave-induced drift $\mathbf{U}_{surf}$,

$$\mathbf{U} = \mathbf{U}_c + \mathbf{U}_{surf}. \tag{10}$$

Note that the total momentum in the mean surface drift equals the total momentum in the Stokes drift.

The conservation laws become (Mastenbroek et al, 1993)

$$\frac{\partial}{\partial t}\zeta + \nabla_h \cdot (h\mathbf{U}) = 0, \tag{11}$$

and

$$\left(\frac{\partial}{\partial t} + \mathbf{U}\cdot\nabla_h\right)\mathbf{U} + g\nabla_h\zeta + \frac{1}{\rho}\nabla_h p_a = \mathbf{U}\times\mathbf{f} + \frac{\tau_a - \tau_b}{\rho h} - \frac{1}{\rho h}\nabla_h\cdot\mathsf{S}, \tag{12}$$

where τ_a and τ_b represent the atmospheric surface stress and the bottom stress. The radiation stress tensor S represents the contribution of the wave motions to the mean horizontal flux of horizontal momentum. In terms of the wave spectrum $F(\mathbf{k})$, which gives the energy distribution of the ocean waves over wavenumber $\mathbf{k}$, the stress tensor is given by

$$\mathsf{S}_{ij} = \rho g \int d\mathbf{k} \left\{ \frac{v_g}{c} l_i l_j + \left(\frac{v_g}{c} - \frac{1}{2}\right)\delta_{ij} \right\} F(\mathbf{k}). \tag{13}$$

Note that the first term corresponds to advection of wave momentum, while the second term consists of a combination of contributions from the wave-induced pressure and the wave-induced stress (Phillips, 1977).

As pointed out by Whitham (1974) the momentum conservation law (12) assumes its most simple form when the mass transport velocity including the wave momentum is used. In this formulation of the conservation laws, ocean waves only appear explicitly through the radiation stress tensor S. Implicitly wave effects also appear through parametrizations of the stress. For example, in case the bottom stress τ_b is modelled in terms of the current velocity $\mathbf{U}_c$ rather than the total velocity $\mathbf{U}$.

Although the depth-averaged continuity and momentum equations show their simplest form in terms of the total velocity, there is a definite need to know the ocean circulation velocity $\mathbf{U}_c$. Following Hasselmann (1971) one obtains the corresponding evolution equations for the current velocity $\mathbf{U}_c$ by eliminating from (12) the rate of change in time of the wave momentum by means of the energy balance equation for surface gravity waves.

The energy balance equation reads (Komen *et al.*, 1996)

$$\frac{\partial}{\partial t}F + \frac{\partial}{\partial \mathbf{x}}\cdot(\mathbf{v}_g F) = S_{in} + S_{nl} + S_{diss} + S_{bot},$$

where $\mathbf{v}_g = \partial\omega/\partial\mathbf{k}$ is the group velocity and ω is the angular frequency. Our discussion will concentrate on the deep water case. Then, the angular frequency obeys the dispersion relation $\omega^2 = gk$, where k is the magnitude of the wavenumber vector. While the left-hand side of the energy balance equation describes advection of wave energy, on the right-hand side there are four source terms that represent the physics of ocean waves. The first one, S_{in} describes the generation of ocean waves by wind and therefore represents the momentum and energy transfer from air to ocean waves. The third and fourth term describe the dissipation of waves by processes such as white-capping, large scale breaking eddy-induced damping and bottom friction, while the second terms denotes nonlinear transfer by resonant four-wave interactions. The nonlinear transfer conserves total energy and momentum and is important in shaping the wave spectrum and in the down-shift towards lower frequencies.

Noting that wave momentum is wave energy divided by the phase speed of the waves, one obtains the rate of change of total wave momentum by dividing the energy balance equation by the phase speed and

by integration over wavenumber $\mathbf{k}$. The result is

$$\frac{\partial}{\partial t}\mathbf{P}^w = -\rho g \nabla \cdot \int d\mathbf{k}\, \frac{\mathbf{l} v_g}{c}\, F + \rho g \int \frac{d\mathbf{k}}{c}\, (S_{in} + S_{nl} + S_{diss} + S_{bot})\,. \tag{14}$$

Substitution of (14) into (12) gives the following evolution equation for the ocean circulation velocity $\mathbf{U}_c$

$$\left(\frac{\partial}{\partial t} + \mathbf{U}_c \cdot \nabla_h\right)\mathbf{U}_c + g\nabla_h \zeta + \frac{1}{\rho}\nabla_h p_a = (\mathbf{U}_c + \mathbf{U}_{surf}) \times \mathbf{f} + \frac{\tau_{oc,a} - \tau_{oc,b}}{\rho h} - \frac{1}{\rho h}\nabla_h \cdot \mathsf{T}, \tag{15}$$

and it is straightforward to rewrite the continuity equation:

$$\frac{\partial}{\partial t}\zeta + \nabla_h \cdot (h\mathbf{U}_c) = -\nabla_h \cdot (h\mathbf{U}_{surf})\,. \tag{16}$$

The conservation laws for the mean ocean circulation differ in a number of respects from the laws for the total current. First, the continuity equation now shows an explicit dependence on the mass flux related to the ocean waves. Second, in the momentum equation effects of the advection of wave momentum have been eliminated, therefore, S is replaced by T with

$$\mathsf{T}_{ij} = \rho g \int d\mathbf{k} \left(\frac{v_g}{c} - \frac{1}{2}\right) \delta_{ij} F(\mathbf{k}). \tag{17}$$

The stress T vanishes in deep water because according to the dispersion relation for surface gravity waves the group speed v_g equals one-half the phase speed c. Thus, only in shallow water there will be a finite contribution, which will be ignored for the moment. Third, the surface stress and the bottom stress are modified accordingly. For example, the surface stress felt by the mean circulation is the total stress minus the net stress going into the waves, or,

$$\tau_{oc,a} = \tau_a - \rho g \int \frac{d\mathbf{k}}{c}\, (S_{in} + S_{nl} + S_{diss})\,, \tag{18}$$

and the bottom stress becomes

$$\tau_{oc,b} = \tau_b + \rho g \int \frac{d\mathbf{k}}{c}\, S_{bot}\,, \tag{19}$$

Fourth, the wave momentum equation (14) does not involve an explicit Coriolis term, and therefore the mean circulation experiences an additional force given by $\rho \mathbf{U}_{surf} \times \mathbf{f}$. It is this additional force, which recently has been given considerable attention.

Since ocean modelling is about evolution of the mean ocean circulation we need to follow the approach suggested by Eq. (15). This means that in the ocean model one needs to introduce the Stokes-Coriolis force while the ocean is driven by the difference between atmospheric stress and the net stress going into the waves.

2.2 Wave breaking and upper ocean mixing

In the past 20 years evidence has been presented on the role of wave breaking and Langmuir turbulence in the upper ocean mixing. Because wave breaking generates turbulence near the surface, in a layer of the order of the wave height H_S, the turbulent velocity is enhanced by a factor of 2-3, while, in agreement with observations there is an enhanced turbulent dissipation. This gives deviations from Monin-Obukhov similarity and the dissipation profile deviates from the usual 'law-of-the-wall'. In addition, an enhanced

transport to the deeper layers of the ocean is possible because work against the shear in the Stokes drift generates Langmuir cells and wave-induced turbulence which has a penetration depth of the order of the inverse of a characteristic wavenumber of the wavefield.

Before sea state effects on the upper ocean mixing are discussed, we briefly describe the 'standard' turbulence model which is based on Monin-Obukhov similarity. Effects of turbulence are modelled by means of a version of the Mellor-Yamada scheme. Here, effects of turbulence on momentum, heat and turbulent kinetic energy are modelled by means of an eddy-viscosity model, where the eddy viscosity ν is proportional to the product of a mixing length $l(z)$, a turbulent velocity $q(z)$ and a factor ST which depends on stratification (as measured by a Richardson number Ri), or,

$$\nu = l(z)q(z)ST(Ri), \tag{20}$$

while the turbulent velocity is obtained from solving the turbulent kinetic energy (TKE) equation. If effects of advection are ignored, the TKE equation describes the rate of change of turbulent kinetic energy e due to processes such as shear production, damping by buoyancy, vertical transport of pressure and TKE, and turbulent dissipation ε. It reads

$$\frac{\partial e}{\partial t} = \nu_m S^2 - \nu_h N^2 - \frac{1}{\rho_w}\frac{\partial}{\partial z}(\overline{\delta p \delta w}) - \frac{\partial}{\partial z}(\overline{e\delta w}) - \varepsilon, \tag{21}$$

where $e = q^2/2$, with q the turbulent velocity, $\mathbf{S} = \partial \mathbf{U}/\partial z$ and $N^2 = g\rho_0^{-1}\partial\rho/\partial z$, with N the Brunt-Väisälä frequency, ρ_w is the water density, δp and δw are the pressure and vertical velocity fluctuations and the over-bar denotes an average taken over a time scale that removes linear turbulent fluctuations. Normally, pressure and TKE vertical transport is ignored, while the dissipation term is taken to be proportional to the cube of the turbulent velocity divided by the mixing length,

$$\varepsilon = \frac{q^3}{Bl}, \tag{22}$$

where, B is a dimensionless constant. Assuming steady state one then obtains the turbulent velocity from the balance between shear production, buoyancy and turbulent dissipation, i.e.

$$\nu_m S^2 - \nu_h N^2 - \varepsilon = 0. \tag{23}$$

The 'law-of-the wall' is now obtained from the reasonable assumption that close to the surface effects of stratification may be ignored while the stress, and hence, the turbulent velocity q is a constant. For a mixing length given by $l(z) = \kappa z$ it then follows immediately from Eq. (22) that close to the surface dissipation increases with the inverse of the distance to the surface.

Sea state effects such as wave breaking and Langmuir turbulence will give rise to considerable deviations from the 'law-of-the-wall'. In order to introduce these sea state effects the TKE equation is extended in the following manner. As suggested by Grant and Belcher (2009) the turbulent production by Langmuir circulation is represented by introducing an additional term that is related to work against the shear in the Stokes drift $\mathbf{u}_S$, i.e. $\nu_m \mathbf{S}\cdot\partial\mathbf{u}_S/\partial z$. Although in principle the depth dependence of the Stokes drift is known theoretically it is computationally very expensive to use the exact expression so we will use the approximate expression

$$\mathbf{u}_S = \mathbf{u}_S(0)\, \mathrm{e}^{-2k_e|z|}/(1+8k_e|z|), \tag{24}$$

where $\mathbf{u}_S(0)$ is the value of the Stokes drift at the surface and k_e is an appropriately chosen wave number scale that both follow from the wave model. For a more detailed discussion see §3.

Furthermore, following Craig and Banner (1994), effects by breaking waves on upper ocean mixing are explicitly taken into account by the introduction of the energy flux from waves to the ocean column. As a consequence, transport of turbulent kinetic energy needs to be introduced as well. It is parametrized by means of a turbulent diffusion model, i.e. $\overline{e\delta w} = \nu_q \partial e/\partial z$. Hence, ignoring the pressure transport, the TKE equation becomes

$$\frac{\partial e}{\partial t} = \frac{\partial}{\partial z}\left(\nu_q \frac{\partial e}{\partial z}\right) + \nu_m S^2 + \nu_m \mathbf{S} \cdot \frac{\partial \mathbf{u}_S}{\partial z} - \nu_h N^2 - \frac{q^3}{Bl(z)}. \tag{25}$$

Craig and Banner now assumed that at the surface there is a direct conversion of mechanical energy to turbulent energy and therefore the turbulent energy flux is assumed to be given by the energy flux from waves to ocean column Φ_{oc} which follows from the dissipation term in the energy balance equation:

$$\Phi_{oc} = -\rho_w g \int d\mathbf{k}\, S_{diss}. \tag{26}$$

Remark that in the absence of relevant information on the sea state the energy flux is often parametrized as $\Phi_{oc} = m\rho_a u_*^3$, where u_* is the air friction velocity while m is in the range of 1-10. The energy flux may also be expressed in terms of the water friction velocity w_* which gives $\Phi_{oc} = \alpha\rho_w w_*^3$ with $\alpha = m(\rho_w/\rho_a)^{1/2}$ having values of the order 30-300.

Hence the boundary conditions become

$$lqS_q \frac{\partial e}{\partial z} = \Phi_{oc}/\rho_w \text{ for } z = 0, \quad \frac{\partial e}{\partial z} = 0 \text{ for } z \to \infty. \tag{27}$$

In the Craig and Banner model turbulent transport of TKE plays an essential role. This follows from an analysis of the TKE equation which reveals that very close to the surface there is a balance between turbulent transport of TKE and dissipation. In fact, from this balance one may obtain the value of TKE at the surface (cf. Mellor and Blumberg, 2004),

$$e(z=0) = \left(\frac{3B}{8S_q}\right)^{1/3} (\Phi_{oc}/\rho_w)^{2/3}, \tag{28}$$

and this is the boundary condition that is usually applied in ocean circulation models, e.g. in the NEMO model. In terms of the water friction velocity the boundary condition for TKE may be written as

$$e(z=0) = e_{bb} w_*^2, \; e_{bb} = \left(\frac{3B\alpha^2}{8S_q}\right)^{1/3}.$$

For old windsea, a typical value for the dimensionless energy flux (in terms of w_*) is $\alpha = 100$ and using from the Mellor-Yamada scheme the standard values $B = 16.6$ and $S_q = 0.2$ one finds that $e_{bb} \approx 68$. This is the default value used in the present NEMO model.

However, the assumption that at the surface there is a direct conversion of mechanical energy into turbulence may be questioned. For example, observations of TKE dissipation in the wave crest region (Gemmrich, 2010) suggest that TKE vanishes at the surface. An alternative approach, which avoids the assumption of direct energy conversion, was suggested by Saetra and Janssen some time ago (Janssen *et al.*, 2004) and this approach was extensively validated (Janssen, 2012) by comparing simulated sea surface temperature with in-situ observations. Thus far, the pressure transport has been ignored but it should be realized that this term may be related to the work done by white capping/wave breaking on the ocean surface. Denoting the negative of the correlation between pressure and velocity fluctuations by

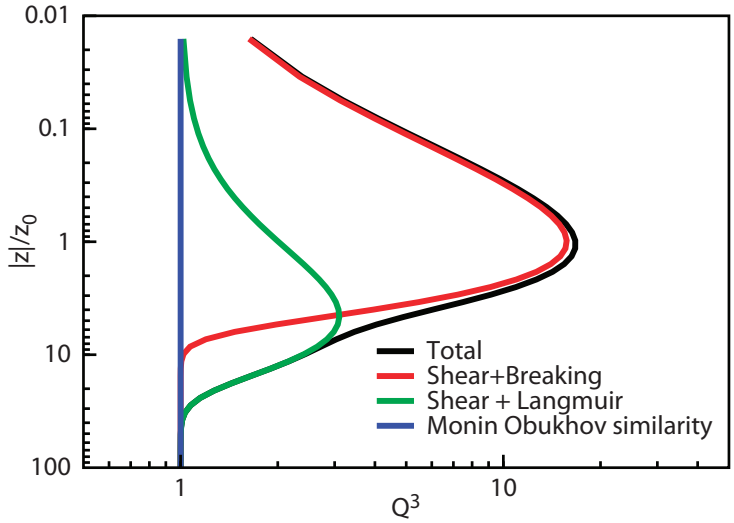

Figure 2: Profile of Q^3 according to the local approximation in the ocean column near the surface. The contributions by wave dissipation (red line) and Langmuir turbulence (green line) are shown as well. Finally, the Q^3-profile according to Monin-Obukhov similarity, which is basically the balance between shear production and dissipation, is shown as the blue line.

$I_w(z)$ it turns out that at the surface the correlation can be written in terms of an integral of the dissipation term in the energy balance equation, e.g.,

$$I_w(0) = -\frac{1}{\rho_w}\overline{\delta p \delta w}(z=0) = \frac{\Phi_{oc}}{\rho_w} = -g\int_0^\infty S_{diss}(\mathbf{k})d\mathbf{k} = m\frac{\rho_a}{\rho_w}u_*^3. \tag{29}$$

The main problem is now how to model the depth dependence of $I_w(z)$, in particular how deep the breaking-induced turbulence will penetrate in the upper ocean. Because breaking is a nonlinear process it is assumed that the depth scale is controlled by the significant wave height H_S (rather then a depth dependence that follows from potential flow). Therefore, the following depth dependence for $I_w(z)$ is suggested:

$$I_w(z) = I_w(0) \times \hat{I}(z),\ \hat{I}(z) = \mathrm{e}^{-|z|/z_0}, \tag{30}$$

where the depth scale $z_0 \sim H_S$ will basically play the role of a roughness length. Based on a comparison between modelled and observed turbulent dissipation, which will be discussed later, we choose

$$z_0 = 0.5H_S. \tag{31}$$

In contrast to the Craig and Banner model one now obtains the following TKE equation

$$\frac{\partial e}{\partial t} = \frac{\partial}{\partial z}\left(lqS_q\frac{\partial e}{\partial z}\right) + \frac{\partial I_w(z)}{\partial z} + \nu_m S^2 + \nu_m \mathbf{S}\cdot\frac{\partial \mathbf{u}_S}{\partial z} - \nu_h N^2 - \frac{q^3}{Bl(z)}. \tag{32}$$

At the surface there is no direct conversion of mechanical energy to turbulent energy and therefore the turbulent energy flux is assumed to vanish. Hence the boundary conditions become

$$lqS_q\frac{\partial e}{\partial z} = 0 \text{ for } z = 0,\ \ \frac{\partial e}{\partial z} = 0 \text{ for } z \to \infty. \tag{33}$$

In this alternative approach some analysis (Janssen, 2012) shows that in the upper part of the ocean the main players are the pressure transport term and the dissipation, while turbulent transport of TKE can

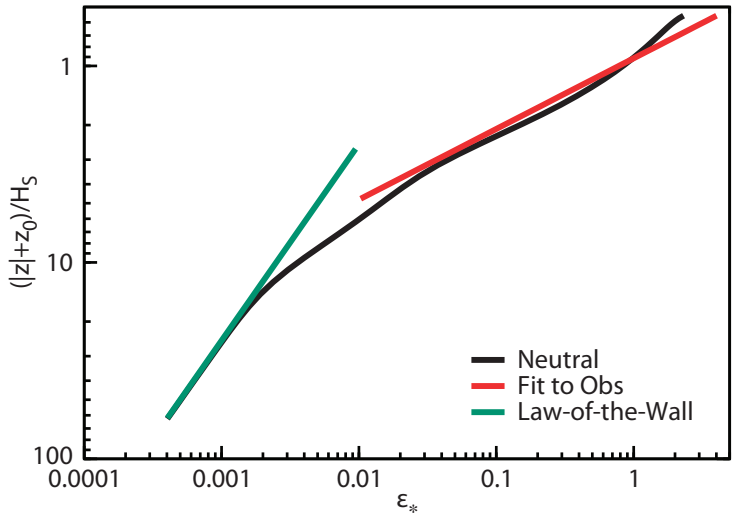

Figure 3: Dimensionless dissipation ε_* versus $(|z|+z_0)/H_S$.

be safely ignored. Without presenting any of the details, for neutral stratification in the steady state, the following '1/3'-rule for the turbulent velocity is then found. Introducing the dimensionless turbulent velocity $Q = (S_M/B)^{1/4} \times q/w_*$ the approximate solution of the TKE equation (32) becomes

$$Q^3 \approx 1 + \alpha\kappa|z|\frac{d\hat{I}_w}{dz} + La^{-2}\kappa|z|\frac{d\hat{U}_S}{dz}, \tag{34}$$

where $La = (w_*/u_S(0))^{1/2}$ is the turbulent Langmuir number which measures the importance of Langmuir turbulence. Therefore, in terms of Q^3 there is a *superposition principle*, so that contributions due to wave dissipation and Langmuir turbulence may be added to the shear production term.

Let us now discuss a 'typical' solution in more detail, namely the one for 'old' windsea. This is a pure windsea state (hence swell is absent) that occurs when a steady wind has been blowing for sufficiently long time so that a steady state has been achieved. A dimensional analysis suggests that the profiles depend on four parameters, namely $\alpha, La, z_0/H_S$, and the integral steepness parameter $s = k_s H_S/2$. We have chosen the typical values $\alpha = 100$, $La = 1/4$, $z_0/H_S = 1/2$ and $s = 0.11$. The approximate solution (34) has been plotted in Fig. 2, while in addition the solution without Langmuir turbulence (in red), without wave breaking (in green) and without breaking and Langmuir (Monin-Obukhov similarity, in blue) have been plotted as well. From Fig. 2 we immediately infer that the maximum in Q^3 by wave breaking is close to the sea surface at a depth z_0 while the maximum by Langmuir turbulence is at the larger depth of $1/2k_s$. These scales are widely different because ocean waves are weakly nonlinear which means that their 'typical' steepness $s = k_s H_S \ll 1$.

The enhanced turbulence in the surface layer is accompanied by deviations from the law-of-the wall, as illustrated in Fig. 3. In this figure we have plotted the dimensionless dissipation $\varepsilon_* = \rho_w \varepsilon H_s/\Phi_{oc}$ as function of the dimensionless depth $Z = (|z|+z_0)/H_S$. For comparison, we have also shown the law-of-the wall which holds for the deeper parts of the ocean. Finally, also shown is a fit that summarizes the observational evidence of dissipation near the surface. The empirical fit is given by (see e.g. Burchard, 2001)

$$\varepsilon_* = 0.78 Z^{-2.78}.$$

We used the fit to the observational data to determine the ratio of the roughness length and the significant wave height, resulting in the choice given in Eq. (31)

2.3 Summary

To summarize, a brief overview has been given of possible sea state effects that may be relevant in a more accurate description of the mixed layer of the upper ocean. Possible candidates are the Stokes-Coriolis force, sea-state dependent forcing and two versions of upper ocean mixing induced by wave breaking. The Stokes-Coriolis force, given by $\rho_w \mathbf{u}_{st} \times \mathbf{f}$, will be added to the ocean momentum equations. Here, the Stokes drift profile $\mathbf{u}_{st}$ is given in Eq. (35). In the case where sea-state dependent forcing of the momentum equation is used the air-side stress τ_a is replaced by the ocean stress τ_{oc} shown in Eq. (18). If sea-state dependent upper ocean mixing is switched on then for option 1 the TKE equation is run using the boundary condition for the energy flux in Eq. 28 while for option 2 the modelled pressure vertical velocity correlation due to wave breaking (see Eq. (29-30) is introduced in the TKE equation, while the energy flux vanishes at the surface.

In the next §'s we will test these candidates by doing standalone runs over a 20 year period using forcing from ERA-interim. Noting that ERA-interim has been produced with a coupled ocean-wave, atmosphere system, the sea state parameters such as Stokes drift, sea-state dependent stress and energy flux from the breaking waves have been explicitly calculated from the archived wave spectra from ERA-interim. As control we use the default version of the NEMO model which uses sea-state parameters valid for 'old' windsea.

As a final remark it is pointed out that there is a nontrivial dependence of parameters such as the momentum flux τ_{oc} and the energy flux Φ_{oc} on the sea state. In order to measure this we remark that in the absence of sea state information one often parametrizes the energy flux as $\Phi_{oc} = m\rho_a u_*^3$ with m having a typical value of 5. Using the wave model, the energy flux can be explicitly evaluated, and it turns out that there is a considerable daily variability in the value of m. In the bottom half of Fig. 4 a map of the dimensionless energy flux m is shown for a two-year period, illustrating that there is a considerable spatial dependence of the dimensionless energy flux as on average in the extra-tropics mixing of the upper ocean is more intense then in the tropics. The reason for this spatial dependence is related to the fact that the age of the sea state (usually measured in terms of the wave age c_p/u_*, with c_p the phase speed of the peak of the spectrum) is younger in the extra-tropics than in the tropics. Younger waves have higher steepness and since wave breaking is nonlinear in the wave steepness there is higher dissipation for young waves than for old waves. This is in agreement with observations from Terray *et al* (1996) and is also found in the ECMWF wave model when the sea state is dominated by windsea.

In the same Figure we also show a map of the monthly mean momentum flux going into the ocean normalized with the air-side stress. Also here some interesting spatial patterns are to be noted, but, to be definite, the variability of the pattern is considerably smaller when compared to the one for the dimensionless energy flux.

The key question to ask now is whether a time and spatially dependent dimensionless normalized momentum and energy flux will result in realistic upper ocean dynamics and mixing. We will try to answer this question in §3 by doing simulations with the NEMO model in which time-varying sea state effects, as obtained from the wave model, have been introduced.

3 Forcing NEMO with wave model fields

Wave model forcing has been implemented in the ECMWF version of NEMO v3.4.1. Here we describe how fields are ingested in *forced mode*, i.e., when NEMO is run in stand-alone mode. Using NEMO in

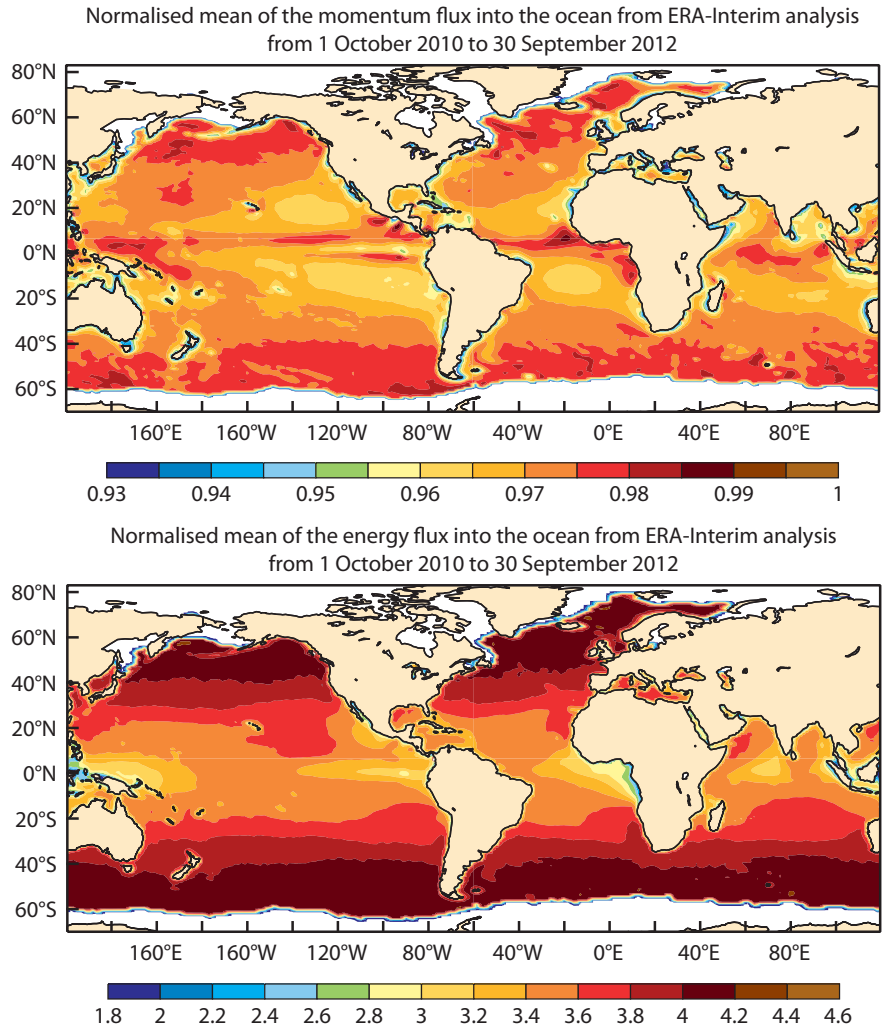

Figure 4: Top: Average of τ_{oc} normalized with the average of the surface stress. Bottom: Average of energy flux into the ocean, normalized with the average of $\rho_a u_*^3$. Averaging period is two years.

forced mode we study the impact of sea state effects in surface stress and upper ocean mixing and we study the impact of the Stokes-Coriolis force on the resulting SST fields. The control run also includes sea state effects, but normally there is no knowledge on the sea state and therefore it is assumed that the sea state is in equilibrium with the wind. This sea state is called 'old' windsea and the energy flux due to breaking waves becomes a simple function of the friction velocity while the ocean surface stress equals the air-side stress.

3.1 Forced mode experiments

A standard experiment setup is adhered to where the model is run for the period 1979-2009 inclusive. All atmospheric forcing fields in the control run (CTRL hereafter) are taken from ERA-Interim (Dee *et al.*, 2011) and are daily averages, while sea state information is provided at six-hourly intervals.

In order to test sea state effects, the 31-yr integrations on 1° resolution (1979-2009) have been conducted using wave parameters from ERA-Interim and have been compared against the control run (CTRL). Two

different vertical resolutions have been tested, ORCA1Z42 with 42 vertical levels and a 10-m thick top level, and ORCA1Z75 with 75 vertical levels and a 1-m thick top level. In addition, all experiments are set up in such a way that there is no data assimilation, SST damping is off, there is a weak 3D damping towards climatology and the LIM2 ice model is switched on.

NEMO forced runs normally require computation of the stress using a bulk formula. In CTRL the surface stress is computed using the ECMWF bulk formula (Edson *et al.*, 2013)

$$C_{D10} = (a + b\Delta U_{10}^{p_1})/\Delta U_{10}^{p_2},$$

where $a = 1.03 \times 10^{-3}$, $b = 0.04 \times 10^{-3}$, $p_1 = 1.48$ and $p_2 = 0.21$, and the relative wind speed $\Delta U_{10} = |\mathbf{U}_{10} - \mathbf{u}_0|$ is found from the difference between the 10-m wind vector and the surface current vector from NEMO. For a discussion of the coefficients that are used in the drag law see Janssen (2008).

WAM computes the air-side stress from the atmosphere into the wave field based on the 10-m neutral wind,

$$\tau_a = \rho_a C_{dw} U_{10N}^2,$$

where C_{dw} is the sea-state dependent drag computed by the WAM model. Hence, this gives the option to compute the air-side stress in NEMO based on the wave-dependent drag coefficient and the 10-m neutral wind. The wind *direction* must still be taken from the atmospheric model, which may lead to minor inconsistencies. We also note here that subtracting the surface current before computing the stress will lead to further inconsistencies. It is however important to remember that these inconsistencies are unique to the forced runs since the coupled runs (to be discussed later) exchange vectorial stresses from WAM.

3.2 The momentum flux from waves into the ocean

As discussed in §2, the ocean feels the water-side stress τ_{oc}. This differs from the air-side stress τ_a by the amount of momentum absorbed ($\tau_{\rm in}$) by the wave field and the amount released from breaking waves ($\tau_{\rm ds}$), or, $\tau_{oc} = \tau_a - (\tau_{in} + \tau_{ds})$.

The absorption in the wave field and the subsequent release to the ocean through dissipation can be related to integrals over the source terms of the wave energy balance equation as shown in Eq. (18), and therefore τ_{oc} can be evaluated, when required.

The water-side stress normalized by the magnitude of the air-side stress, $\tau_{\rm a}$, is archived in ERA-Interim. Using the water-side stress gives differences in SST compared with CTRL, which are shown in Fig.A1 of Appendix A. The most persistent differences are found along the eastern edge of the Pacific where the modifications to the wind stress appear to lead to reduced upwelling. A cooling of up to 0.5 K is found in the Gulf Stream and Kuro-Shio regions. The eastern tropical Pacific experiences a slight warming. A comparison against all available SST observations (OIv2, Reynolds *et al.*, 2002), as shown in Fig. A2, gives a slight reduction in the SST bias when compared with the bias in the CTRL.

3.3 Impact of Stokes-Coriolis force

The Stokes-Coriolis force has been implemented as a tendency to the momentum equations in NEMO. The surface Stokes drift is taken from the ERA-Interim archive and an approximate Stokes-drift profile is used to estimate the transport caused by the Stokes-Coriolis force.

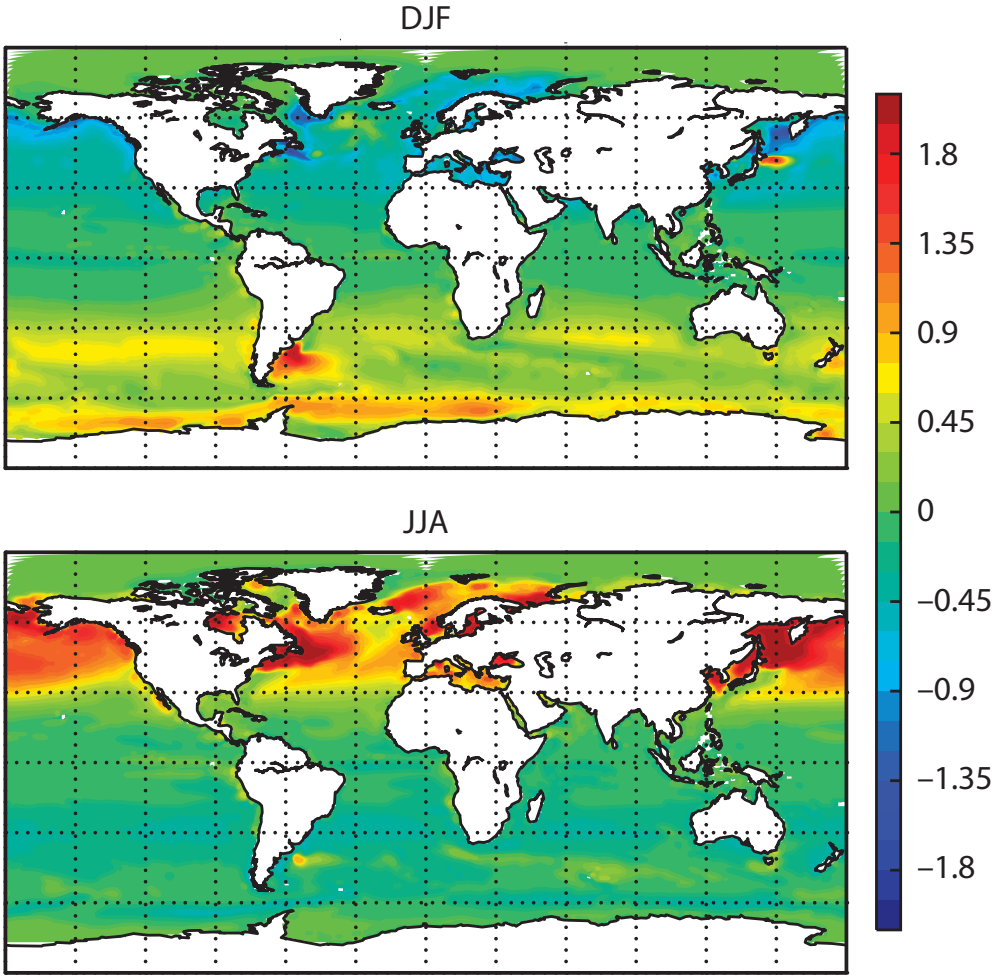

Figure 5: 20-yr average SST difference between CTRL and a run with TKE mixing dictated by the energy flux from the ERA-Interim WAM model plus the other wave effects. The differences are most pronounced in the summer hemisphere, where the mixing is reduced, leading to higher SST. The colour scale is ±2 K.

In the deep-water limit, where the dispersion relation for water waves is given by $\omega^2 = gk$, the Stokes profile can be written as

$$\mathbf{u}_{st}(z) = 2\int d\mathbf{k}\,\omega\,\mathbf{k}\,\mathrm{e}^{2kz}\,F(\mathbf{k}). \tag{35}$$

Determining the full Stokes profile from Eq. (35) is expensive, and when the wave spectrum is not available the profile must be approximated in such a way that the surface Stokes drift vector $\mathbf{u}_0$ and the Stokes transport $\mathbf{T}_{st} = \int_{-\infty}^{0} \mathbf{u}_{st}(z)\,dz$ are given correctly. In the deep-water limit the Stokes transport becomes

$$\mathbf{T}_{st} = \int d\mathbf{k}\,\omega\,\hat{\mathbf{k}}\,F(\mathbf{k}). \tag{36}$$

The integrand here is the first moment of the variance spectrum, m_1, weighted by the unit vector $\hat{\mathbf{k}}$ of the wave component.

Because of the computational cost and often also due to lack of access to the full two-dimensional wave spectra it is customary (see e.g. Rascle *et al.*, 2006, Saetra *et al.*, 2007) to approximate Eq. (35) by the

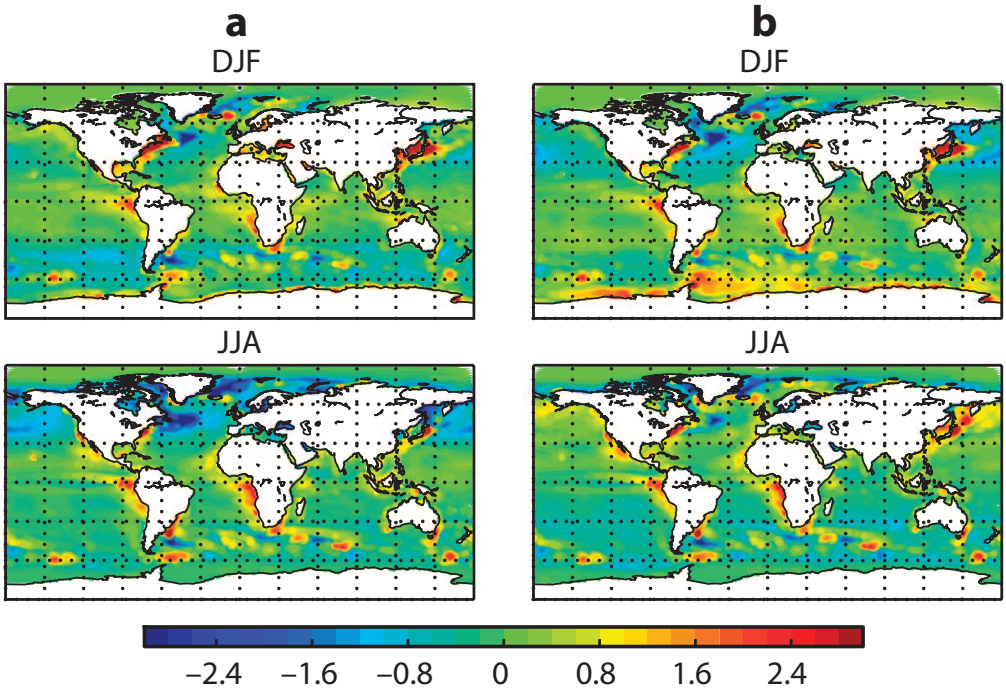

Figure 6: Panel a: 20-yr average SST difference between CTRL and OIv2. Panel b: difference between a run with TKE mixing dictated by the energy flux from the ERA-Interim WAM model and OIv2, giving smaller biases in the summer hemisphere.

exponential profile of a monochromatic wave,

$$\mathbf{u}_m = \mathbf{u}_0 \, \mathrm{e}^{2k_m z}.$$

We have found that an alternative to the exponential profile of the form

$$\mathbf{u}_e = \mathbf{u}_0 \frac{\mathrm{e}^{2k_e z}}{1 - 8k_e z}. \tag{37}$$

yields a closer agreement with the full profile than the monochromatic approximation. The transport under such a profile can be obtained analytically and involves the exponential integral E_1 (Abramowitz and Stegun, 1972,**5.1.28**). It becomes

$$|\mathbf{T}_{st}| = \frac{|\mathbf{u}_0| \mathrm{e}^{1/4} E_1(1/4)}{8k_e}$$

and by inverting this equation one obtains the effective wavenumber k_e as function of the Stokes drift at the surface and the Stokes transport, or,

$$k_e = \frac{|\mathbf{u}_0| \mathrm{e}^{1/4} E_1(1/4)}{8|\mathbf{T}_{st}|} \approx \frac{|\mathbf{u}_0|}{5.97|\mathbf{T}_{st}|} \tag{38}$$

In a similar manner an expression for the typical wavenumber k_m of the monochromatic case can be obtained with the result that $k_m = |\mathbf{u}_0|/2|\mathbf{T}_{st}|$, implying that with the new, more accurate approximation (37) an increase in penetration depth by about a factor of 3 is found. Therefore, with the profile (37) Stokes-Coriolis effects are felt to much greater depth.

Finally, the Stokes transport is estimated from spectral information in the following manner. Introduce the mean angular frequency $\overline{\omega} = m_1/m_0$ and the significant wave height $H_S = 4\sqrt{m_0}$, then the following estimate of the Stokes transport may be found:

$$\mathbf{T}_{st} = \frac{1}{16}\overline{\omega} H_S^2 \hat{\mathbf{k}}_s. \tag{39}$$

Here $\hat{\mathbf{k}}_s = (\sin\theta_s, \cos\theta_s)$ is the unit vector in the direction θ_s of the Stokes transport.

The NEMO implementation computes the Stokes-Coriolis force and adds it to the momentum equation at the appropriate U and V points as a tendency. Contributions below 150 m are ignored because at those depths the Stokes drift is vanishingly small, even for strong wind speeds (for old windsea the Stokes profile has an e-folding depth of $(2k_e)^{-1} \approx 0.03U_{10}^2$, which for a 20 m/s wind equals 10 m). For real profiles the presence of swell may substantially increase the penetration depth, but even accounting for long swell a cutoff at 150 m depth is sufficient.

The effect of the Stokes-Coriolis forcing on SST is mainly seen in the extratropics, which is natural since it scales with the Coriolis frequency. The differences are on the order of 0.5 K compared with CTRL as can be seen in Fig. A3.

3.4 Impact of energy flux from waves on SST

The energy flux from breaking waves to the ocean is described in Sec 2.2. The implementation in NEMO also takes into account the thickness Δz of the uppermost model level.

If we assume, as do Craig and Banner (1994) and Mellor and Blumberg (2004), that in the uppermost, wave-affected layer, the roughness length can be set to a constant which we choose to be $z_w = 0.5H_S$ and that in this near-surface region diffusion balances dissipation, then Eq. (25) has the simple solution

$$e(z) = e_0\, \mathrm{e}^{z/z_{cb}},$$

where the decay length scale for TKE is given by

$$z_{cb} = \frac{1}{2} S_q B \kappa^2 z_w.$$

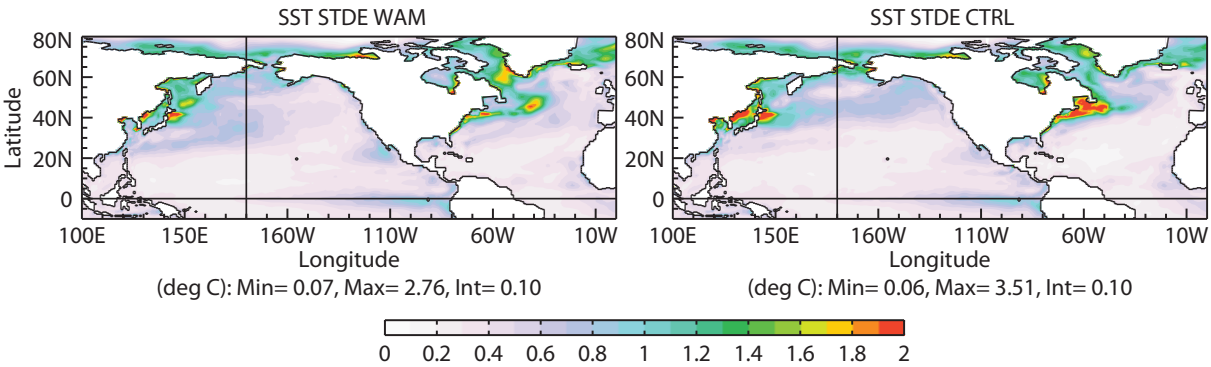

Figure 7: Standard deviation of errors in modelled SST, obtained from a comparison with OIv2 SST analyses.The left panel, labeled WAM, shows the STD errors when all sea state effects are switched on, while the right panel shows the STD errors obtained from CTRL.

It turns out that this decay length scale is quite small. For the parameters $S_q = 0.2$ and $B = 16.6$, as used in NEMO, one finds $z_{cb} \sim z_w/4$. For a wave height of 2.5 m, which is close to the global mean, the typical value of z_{cb} becomes of the order of 0.5 m.

In the present versions of NEMO the boundary condition (28) is applied, i.e. the value of TKE at the surface is specified. However, when TKE is varying rapidly in comparison to the coarse resolution in the vertical a too large mixing of the upper layer will result. It was therefore decided to use the average TKE as boundary condition at the surface. The average TKE for the uppermost level with thickness Δz is given by,

$$e_1 = e_0 \frac{z_{cb}}{\Delta z}\left(1 - \mathrm{e}^{-\Delta z/z_{cb}}\right)$$

which will differ substantially from the surface value for a thick uppermost level, such as ORCA1Z42 has.

Fig. 5 compares a run with all wave effects included (TKE from breaking waves, modified stress and Stokes-Coriolis forcing) to the CTRL run. We see a substantial increase in the SST in the summer hemisphere due to reduced mixing when comparing with the CTRL run.

The changes to SST when comparing with OIv2 SST analyses are generally in the right direction, although there are notable regions where CTRL is closer to the observations (Fig. 6). In addition, as shown in Fig. 7, there are marked reductions in the standard deviation of error of SST when the above sea state effects are switched on, in particular in the Gulfstream area and near the Kuro-Shio current. A comparison with *in situ* observations has been done, and globally temperature biases in the mixed layer are reduced somewhat (Fig. A4), although much more at 25-50 m depth than at the surface. Finally, impact of sea-state dependent mixing is found down to 400 m depth as illustrated by a cross section at 170 E of the temperature difference between experiment and CTRL shown in Fig. A5.

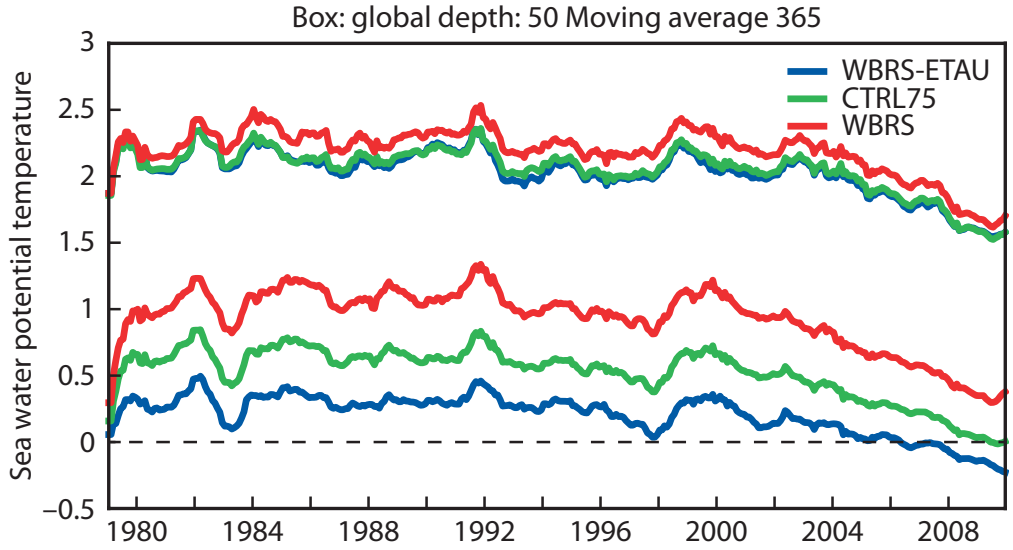

Figure 8: Time series of global model bias (lower curves) and standard deviation (upper curves) for observed temperature at 50 m depth globally (CTRL=green, WBRS-ETAU=blue, WBRS=red). Here WBRS includes mixing by wave breaking and unresolved surface wind variability while in WBRS-ETAU effects of unresolved surface wind variability are switched off. The range in biases gives an indication of the sensitivity to the additional mixing by the unresolved variability.

3.5 Wave breaking as a source term to the TKE equation

As outlined in Section 2.2, the injection of TKE from breaking waves can also be formulated as a source term to the TKE equation. In this case we must change the upper boundary condition accordingly. We have implemented this as an option in NEMO where the TKE from breaking waves is added as a tendency to the TKE equation. The *e*-folding depth is $z_0 = 0.5H_s$ and we can therefore safely confine the computation to the model levels in the upper 50 m of the ocean.

A number of experimental runs have been carried out with the source term formulation, and the preliminary conclusion is that it may prove a useful alternative for a 75-level model with a 1-metre thick uppermost level, but for a 42-level model we expect the flux boundary condition of Craig and Banner (1994), modified by using the average TKE at the surface, to work better.

However, for a 75-level model adding the source term may allow us to remove the additional mixing induced by unresolved surface wind variability (controlled by the `nn_etau` namelist variable). This has garnered some interest in the NEMO community recently as it adds in an *ad hoc* manner TKE to the lower levels based on the surface value to boost the mixing. Fig. 8 shows the sensitivity range to the additional mixing induced by `nn_etau` at 50 m depth. It is also interesting to note that the bias at this level is significantly reduced with a combination of a wave breaking source term and no additional mixing (blue curve). At the moment, it is too early to decide which of the two ways of injecting TKE will prove more beneficial in a future 75-level model setup.

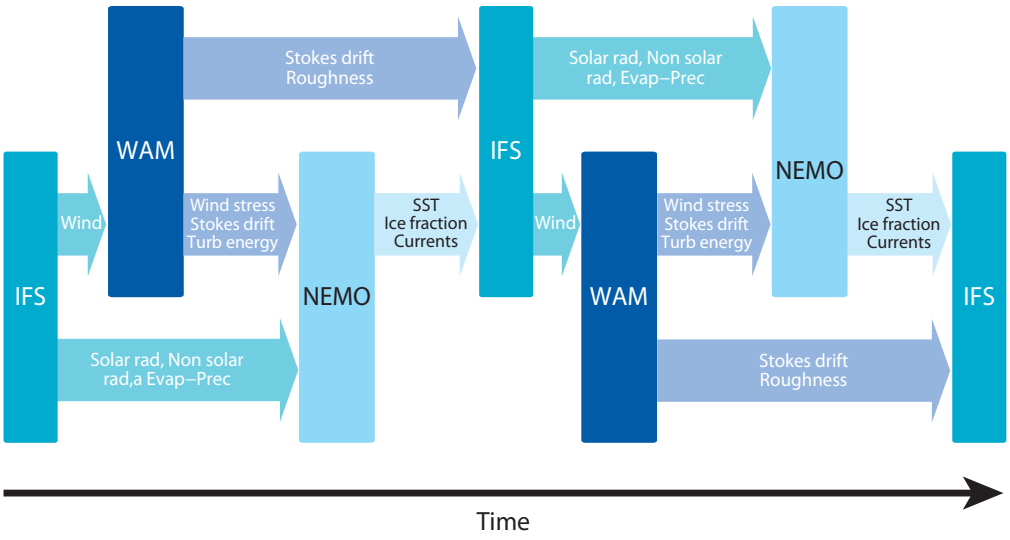

Figure 9: Flow chart of the coupled model, here two time steps are shown.

4 Coupled Simulations

After studying results with the standalone version of NEMO in forced mode we will now discuss results obtained with a coupled IFS-WAM-NEMO system on a seasonal timescale. First, some details of the coupled system are described, followed by a presentation of results obtained from the coupled simulations. In particular, impact of sea state information on the mean state and on the skill of seasonal forecasts is studied.

4.1 Description of the single executable coupled system

In the newly developed coupled atmosphere-wave-ocean system all components are integrated into the same executable with a sequential calling of each components. In the simplest configuration, without an active sea ice model in ocean component, the call sequence is as follows:

1. The atmospheric model (IFS) runs for one coupling time step and produces an updated wind field for the wave model (WAM) as well as updated radiation (solar and non-solar) and evaporation minus precipitation fields for the ocean model (NEMO).
2. WAM runs for the same period and produces updated sea surface roughness for atmosphere model and updated Stokes drift, and turbulent kinetic energy (Φ_{oc} in section 2.2) for the ocean model (NEMO).
3. NEMO runs for the same period and produces updates sea surface temperature and surface currents as input to the IFS model.

After the call to the NEMO model the cycle repeats itself. The flow chart of the coupled model is given in Fig. 9.

It is possible to have different periods for the different model components. For example, for the atmospheric model running at T255L91 with a 45 minutes timestep we can exchange data with the ocean model running at ORCA1L42 resolution with a 1 hour time step every 3 hours by running the atmosphere model for 4 time steps before we run the ocean model for 3 time steps. More details on the single executable coupled system can be found in Mogensen *et al.* (2012).

4.2 Results of the coupled simulations

To test the effects of including the wave coupling a series of three experiments was performed. One experiment was done with the reference settings of the NEMO v3.4.1 TKE scheme (CTRL hereafter), another experiment was done with a change to the e_{bb} parameter, reducing the magnitude of the surface value of TKE, from 67.83 to 20.0 (TKE-20), and finally an experiment was done where both the sea state dependent mixing and the Stokes-Coriolis effect were activated (TKE-WAM).

The reasons to perform the additional experiment TKE-20 are the following. In §3.4 we have noted that imposing a surface boundary condition on TKE gives rise to too much mixing if an ocean model with a thick uppermost layer is used. This is because TKE, as induced by wave breaking, varies quite rapidly with depth. Therefore we introduced a modification to NEMO where instead of the surface value we impose the average TKE over the uppermost layer. This average depends, however, on the sea state. As an alternative solution, we did forced mode experiments where we reduced the surface value to such an extent that biases in SST are minimal. It turned out that for 42 vertical levels $e_{bb} = 20$ gave a satisfactory solution (but note that the optimal value depends on the vertical resolution).

For all experiments CY39R1 of the coupled model was used with an atmospheric resolution of T255L91 and using the ORCA1 configuration with 42 vertical levels for the NEMO model. The runs were based on the seasonal forecasting setup with 3 ensemble members with a forecast length of 7 months starting from the 1st May and the 1st November from 1981 to 2010 equalling a total of 60 start dates. No stochastic physics was used in these runs so the difference between ensembles members was created by choosing different ocean ensemble members from the ORAS4 ocean reanalysis and from the application of SST perturbations at initial time.

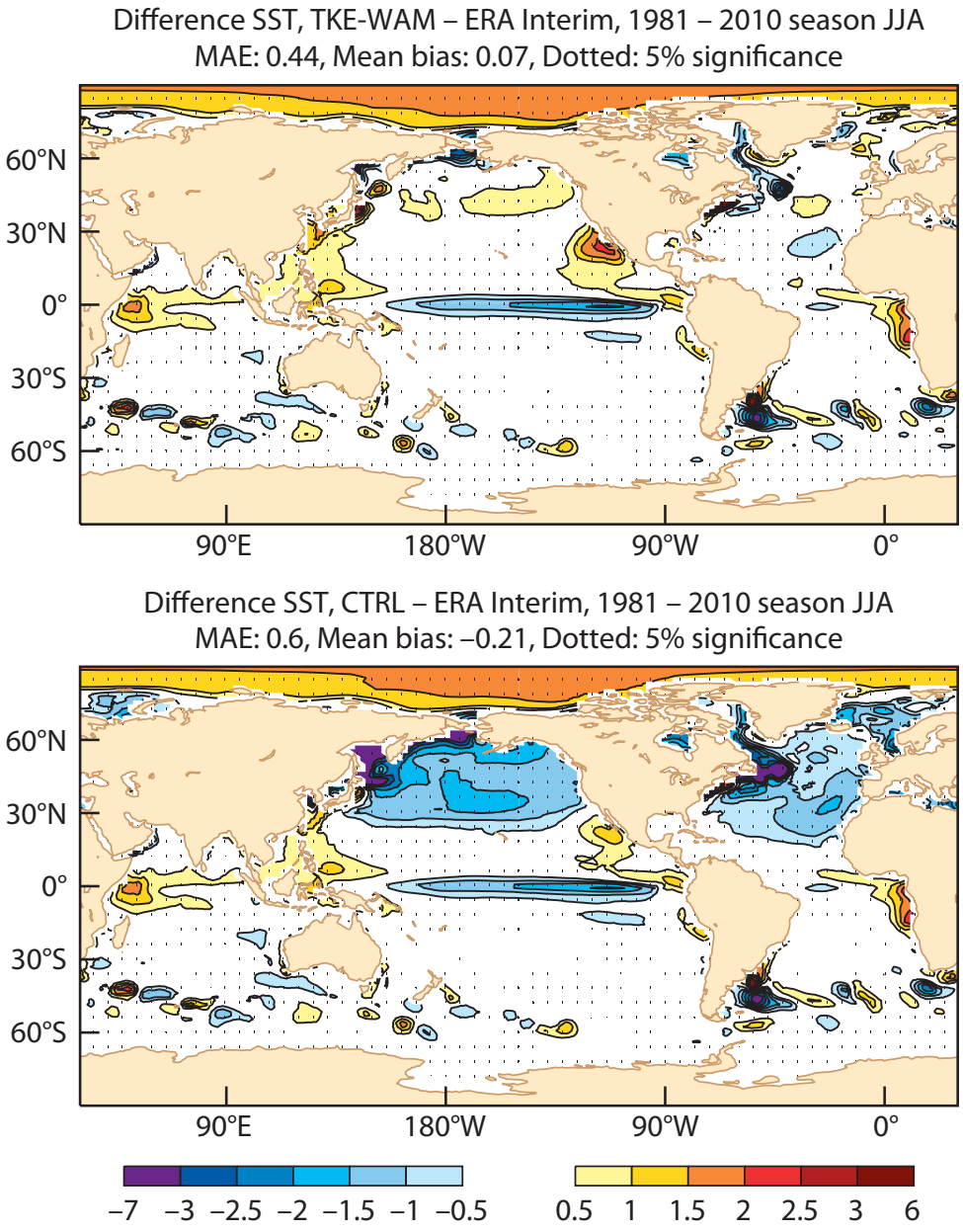

Figure 10: Systematic differences in SST with respect to the OIv2 analysis for JJA with start dates in May. Top panel the experiment TKE-WAM, bottom panel the CTRL experiment.

Impact on the mean state

Figure 10 shows the SST bias for the seasonal experiments initiated in May for JJA. The CTRL experiment shows a pronounced cold bias at high latitudes in the summer hemisphere, in both the Pacific and the Atlantic basins. For November starts, the cold bias appears in the Southern Hemisphere, not shown. In experiment TKE-WAM, where the TKE input is obtained directly from the wave model, the cold bias disappears, especially in the Atlantic basin, while in the Pacific a weak warm bias is now present. The

warm bias in the eastern part of the Pacific basin, associated with the weak coastal upwelling and poor representations of the stratocumulus, which was weak in CTRL, appears enhanced when the TKE input is from the waves, suggesting that in CTRL there might have been compensation of errors. Both experiments exhibit a pronounced cold tongue bias, slightly reduced in the TKE-WAM only for November starts (see later in Fig 11), and a warm bias in the Western tropical Pacific and Indian Ocean. There is little impact on SST in the winter hemisphere.

The different mean state in SST impacts the mean atmospheric circulation, with experiment TKE-WAM showing a reduced (improved) mid-latitude circulation in response to weaker meridional gradients in SST, with a weaker summer-time subtropical high (not shown).

The experiment TKE-20 shows very similar SST as experiment TKE-WAM and is therefore not shown.

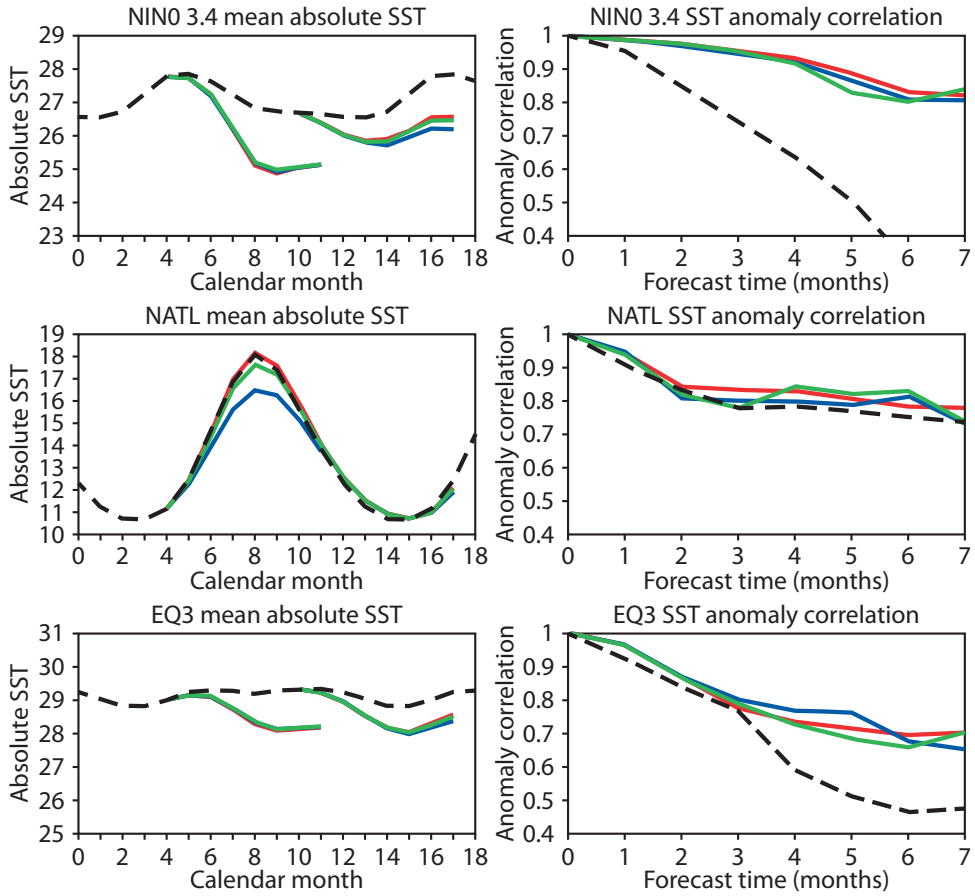

Figure 11: Absolute SST (left column) and correlation (right column) for the seasonal forecasts with CTRL (blue), TKE-WAM (red) and TKE-20 (green) in selected areas: NINO3.4 (170W-120W, 5N-5S), North Atlantic (30N-60N), Equatorial Western Pacific (region EQ3, 150E-170W, 5N-5S). In the left column results are compared with observations (dashed black), while the anomaly scores on the right are compared with persistence (dashed black).

Impact on seasonal forecasts

The skill of seasonal forecast of SST has been estimated for the different experiments above. Although the number of ensemble members is small (only 3) there are a substantial number of starting dates. Nevertheless the following results should be considered preliminary. Fig. 11 shows the absolute SST (left column) and correlation (right column) for the seasonal forecasts with CTRL, TKE-WAM and TKE-20 in different areas. Results show that TKE-WAM has some positive impact on the anomaly correlation skill over the Central Pacific (NINO3.4, 170W-120W, 5N-5S) and North Atlantic (30N-60N), and a slight degradation in the Equatorial Western Pacific (region EQ3, 150E-170W, 5N-5S). In other regions the impact of the TKE modifications on forecast skill is not so clear.

It is interesting to notice that the improvement in NINO3.4 is only apparent with TKE-WAM and not with TKE-20, in spite of the fact that both have a similar mean SST. In the North Atlantic, TKE-WAM is the best in reproducing the amplitude and phase of the seasonal cycle of the SST, followed by TKE-20, since the latter slightly underestimates the summer warming. The seasonality is substantially weaker in the CTRL experiment. The usual expectation is that the improved mean state is associated with improvements in skill, but this is not easy to demonstrate, and it is definitively not the case for the experiment TKE-20. However, it should be realized that the anomaly scores are obtained from SST's that have been corrected for the model drift shown in the left column of Fig. 11. This could therefore very well mask improvements in skill caused by improvements in the mean state.

Finally, the explanation of the fact that both TKE-WAM and TKE-20 appear to degrade the skill in the Equatorial Western Pacific remains unknown. It may be related to the slightly increased easterly bias in wind in TKE-WAM with respect to the CTRL (not shown). However, the level of wind and SST variability in all experiments is very similar. This result is surprising, since, compared to CTRL, both the TKE-WAM and the TKE-20 experiments do not seem to degrade the mean state in SST, but their skill scores are slightly worse compared to CTRL. This needs to be investigated further.

5 Coupling from Day 0

In the present operational medium-range/monthly ensemble forecasting system the forecast range is split in two parts, called leg A and leg B. In leg A, which consists of the first 10 Days of the forecast, the atmospheric model has high resolution while the ocean is passive. In Leg B the atmospheric model has half the resolution while the ocean becomes an active part of the coupled system. It is therefore of interest whether there are further benefits in forecasting by coupling the atmosphere with the ocean from initial time. In this section we list, based on numerical simulations, a number of a advantages of coupling from Day 0. This two-way interaction turns out to be beneficial for forecasting slowly moving hurricanes, it improves the prediction of the MJO and some definite improvements in the statistical skill scores of ENS are found, in particular in the tropics.

The ocean model used in the ENS experiments is NEMO v3.4.1 with sea-state dependent TKE (Option 1) and Stokes-Coriolis forcing activated. In NEMO v3.4.1 the sea-state dependent stress τ_{oc} gave due to interpolation errors occasionally noisy results and therefore it was switched off for security reasons. This has since been corrected. The default light penetration scheme of v3.4.1 consists of three bands and includes the mean effects of chlorophyl. In upwelling areas this scheme resulted in a considerable overestimation of SST and therefore we reverted to a 2-band penetration scheme which is the scheme used in operations.

The ocean model used in the experiments testing the impact of coupling on hurricanes and on the forecast of the MJO was an earlier version of NEMO which did not include sea state effects on upper ocean mixing while for the atmosphere Cy38R1 was chosen. It is strongly emphasized that in this § the principal interest is in testing whether coupling from Day 0 is beneficial, we have not studied in detail whether sea state effects in upper ocean mixing and the introduction of the Stokes-Coriolis force have impact on the medium-range and monthly time scales.

5.1 Impact on hurricanes

Recent studies have shown that in certain circumstances, the ocean can have impact on hurricane intensification (Shay *et al.* 2000; Moon et al. 2007; Yablonski and Ginis 2008; Shay and Uhlhorn 2008). The wind circulation associated with a hurricane tends to reduce the sea surface temperature below the hurricane by several degrees. The cooling of sea surface is then likely to weaken the intensity of the hurricane, because the heat flux reduces. This feedback effect is expected to be stronger for slowly moving hurricanes.

In ENS the IFS is forced by persisted SST anomalies during the first 10 days of integrations. As a consequence, the air-sea interaction described above is not simulated by the model during the first 10 days of integrations, and this may result in an overestimation of the intensity of some hurricanes. This was indeed the case for hurricanes Nadine and Leslie during the 2012 Atlantic hurricane season. To evaluate the impact of coupling IFS to ORCA1L42 NEMO on the intensity of hurricanes, 15-day ENS forecasts of Leslie and Nadine have been reproduced with the same setup as in operations, but with IFS coupled to NEMO during the first 10 days of integrations. The forecast starting dates are 19 September 2012 for Nadine and 3 September 2012 at 12 UTC for Leslie. In both cases, the coupled integrations produce a significant cooling of SSTs below the hurricane. For instance Fig. 12 shows the difference of ensemble mean SSTs between day 5 and day 0 in the coupled integrations starting on 19 September 2012 (Nadine case). This Figure shows an extensive area over the North Atlantic with cooler SSTs at day 5. The amplitude of the cooling reaches 2.5°C over some areas near the centre of hurricane Nadine. As illustrated in the bottom part of Fig. 12, the intensity of Nadine is weaker in the coupled integrations than in the control integrations (ensemble mean maximum sustained wind of 26.5 m/s in the coupled integrations instead of 30.9 in the uncoupled integrations and a mean sea level pressure of 979 hPa in the coupled integrations instead of 971 hPa in the ensemble mean). The difference of hurricane intensity between the coupled and uncoupled integrations is statistically significant within the 1% level of confidence. The intensity of Nadine in the coupled integrations is closer to observations (observed mean sea level pressure of 978 hPa) than in the uncoupled integrations.

Leslie is another example of a slow moving hurricane during the 2012 Atlantic hurricane season. The operational EPS overestimated strongly its intensity. For instance, the ENS forecasts starting on 3 September 2012 predicted a mean sea level pressure of 957 hPa, which is 13 hPa lower than the observed mean sea level pressure (970 hpa). ENS integrations coupled from day 0 predict a mean sea level pressure of 968 hPa (ensemble mean), which is very close to the observed value. The difference of hurricane intensity between the coupled and uncoupled ENS integrations is statistically significant within the 1% level of confidence. As for Nadine, there is no significant difference in the tracks of the hurricane between both experiments.

Coupled experiments have also been performed for other tropical storms during the 2012 Atlantic season, showing in general little impact. Coupling from Day 0 had no significant impact on the intensity of Sandy, but the experiment with coupling from Day 0 displays higher hurricane strike probability over New York than the uncoupled experiment (not shown).

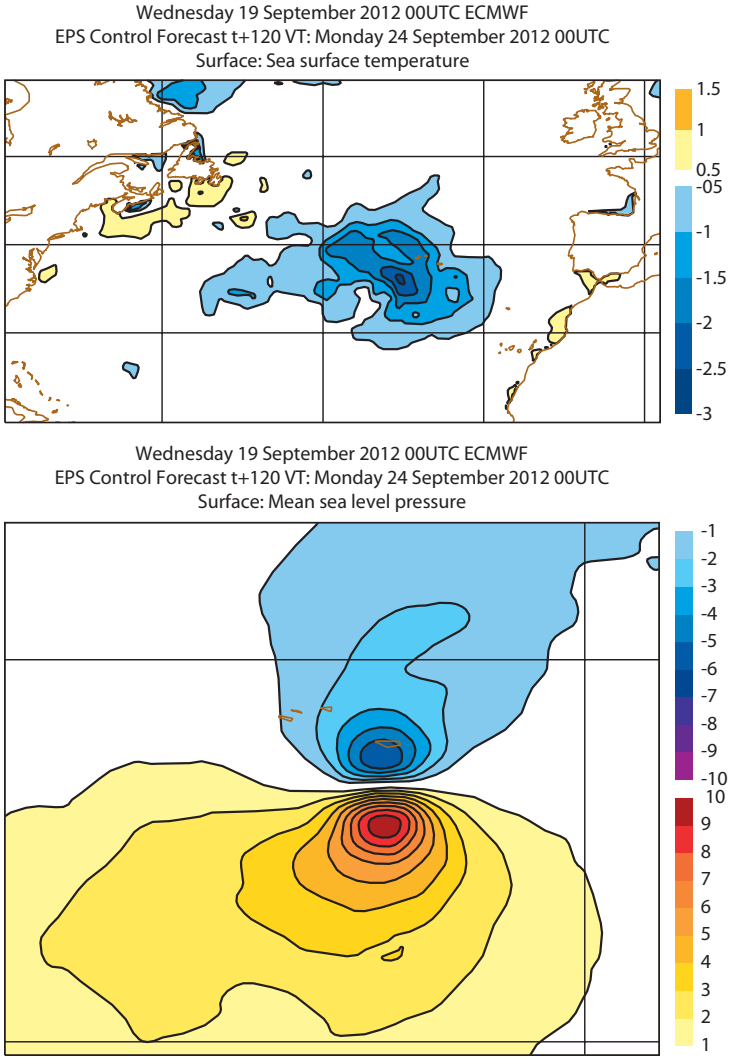

Figure 12: **Top***: Ensemble mean SST difference between day 5 and day 0 from the 51-ensemble integrations starting on 19 September 2012 with IFS coupled to NEMO with 1° resolution during the first 10 days of the integrations.* **Bottom***: Difference in ensemble mean surface pressure between coupled and control for the 5 day forecast from 19 September 2012.*

5.2 Impact on the MJO

Another justification for including an interactive ocean below the atmospheric model from Day 0 is the impact of the ocean-atmosphere interactions on the propagation of the Madden-Julian Oscillation (MJO) (see Woolnough et al 2007 for instance) which is a main source of predictability in the tropics on the sub-seasonal time scale. In order to assess the impact of ocean-atmosphere coupling in the current operational ENS configuration, a series of re-forecasts has been produced with and without coupling from Day 0. The re-forecasts consist of a fifteen-member ensemble of 45-day integrations starting on the 1st February, May, August and November 1989-2008 with IFS cycle 38R2. The MJO is diagnosed by projecting each ensemble member onto the two leading combined Empirical Orthogonal Functions (EOFs) of zonal winds at 850 hPa and 200 hPa and outgoing long-wave radiation (OLR) averaged between 15N and 15S (Wheeler and Hendon, 2003, Gottschalk et al, 2010). The skill of the monthly forecasting system is then estimated by computing the anomaly correlations of principal components 1 and 2 (PC1 and

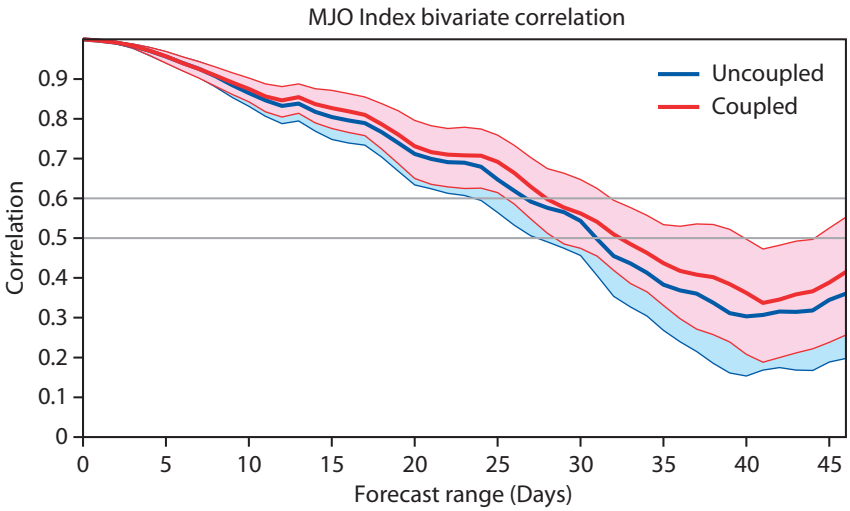

Figure 13: MJO Bivariate correlation for the control runs (leg A uncoupled, blue curve) and coupled from day 0 integrations (leg A coupled, red curve). The shaded areas represent the 5% level of confidence using a 10,000 re-sampling bootstrap procedure.

PC2) predicted by the model with the PC1 and PC2 computed from the analysis (in this case ECMWF reanalysis dataset, ERA-Interim). Fig. 13 suggests that model integrations with leg A coupled from Day 0 display higher skill in predicting the MJO than the control runs. The gain in skill is about 1 day of predictive skill.

5.3 Impact of coupling on ENS in the medium-range

An overview is given here of the impact of coupling from initial time using ENS with the configuration that is planned to be implemented. Two ENS experiments have been run using model cycle 39r1. Experiment $\mathscr{C}$ is coupled from initial time, while experiment $\mathscr{P}$ uses persisted SST anomalies in leg A, i.e. up to Day 10. In leg B of experiment $\mathscr{P}$, the IFS is coupled to NEMO. The initial conditions for leg B are obtained by forcing the ocean model with the wind stresses of the leg A integration. This corresponds to the coupling configuration of the operational ENS configuration in cycles prior to 39r1. Experiment $\mathscr{C}$ uses tendency coupling during the first five days. Then, between Day 5 and Day 9, the observed SST anomalies are decreased leading to full coupling from Day 9.

Apart from the differences in the ocean-atmosphere coupling in leg A the two experiments are identical and the configuration corresponds to the one planned for operational implementation in cycle 40r1. This cycle includes a revision of the physics with a change to the representation of the vertical turbulent fluxes in the atmosphere. Furthermore, the vertical discretisation changes from 62 levels with a model top at 5 hPa to 91 levels with a top at 1 Pa. The horizontal resolution is as in the operational ENS with truncations T_L639 and T_L319 in leg A and leg B, respectively. The ENS consists of 50 perturbed forecasts and one unperturbed control member. The experimentation covers 33 cases in a boreal winter period (10 January to 14 March 2012) and 28 cases in boreal summer period (6 June to 13 August 2012).

First, noticeable changes to the SST errors are presented. Thereafter, the impact on upper air scores in the medium-range is summarized.

Sea surface temperature

Replacing the persisted SST anomalies in leg A by the coupled model may lead, because of model drift, to larger systematic errors. This is obvious as the persisted, observed SST anomalies are by definition unbiased for a large sample when compared to the observed data set. On the other hand, the random errors of the persistence forecast increase with lead time and there is the potential that the coupled model forecast is overall more accurate than the persistence forecast in regions that evolve significantly during the first ten days. Therefore the key question is whether the benefit of the latter outweighs the degradation due to the increased bias.

Fig. 14a and b show the mean SST error of the 10-day ensemble mean for experiment $\mathscr{C}$ and $\mathscr{P}$, respectively. For experiment $\mathscr{P}$, the bias in the mean state is small and not statistically significant, as expected. For experiment $\mathscr{C}$, we see many different structures and many of them are small scale. The regions east of North America and Japan stand out because the positions of the boundary currents are not well reproduced by the model, leading to increased systematic errors. The eastern equatorial Pacific starts to develop a cold bias in the coupled model, which corresponds to the early phase of the "cold tongue problem", which for the ECMWF coupled model is discussed in e.g. Magnusson et al. (2012). Finally, a warm bias starts to develop in Southern Ocean, south of 55S, in agreement with the systematic errors found in the standalone runs of §3.

Fig. 14c shows the day-10 difference between experiment $\mathscr{C}$ and experiment $\mathscr{P}$ of the ensemble mean absolute error which is a measure of RMS error. Negative values indicate improved forecast quality. In the extended tropical region (30N–30S), the SST forecasts are generally improved by introducing the coupling from Day 0. The largest improvement is found west of the Maritime continent, which could be related to the interaction between MJO and SSTs. Improvements are also found west of South America that can be related to better interaction between the atmospheric winds and/or cloud and upwelling of cold water in the ocean. For the northern extratropics, we see a degradation of the forecast quality along the boundary currents as expected from the increase in the systematic errors.

Tropospheric ensemble skill

The continuous ranked probability score (CRPS) has been computed for a set of tropospheric variables (500 hPa geopotential, temperature and wind at 850 hPa and 200 hPa) to quantify the impact on the ensemble skill. The verification is against the analysis produced by the 38r2 rd e-suite. As the results for the boreal summer and the boreal winter periods are similar, we focus on the combined sample of 61 cases.

Scores in the extratropics display a neutral to small positive impact of coupling from initial time. Fig. 15 shows the CRPS of 500 hPa geopotential in the northern extratropics (20N–90N). A more substantial impact is evident in the tropics (Fig. 16). At later lead times, there is a considerable positive impact on the ensemble skill which is generally statistically significant after about day 7. There is also a minor negative impact in the lower troposphere at early lead times. This may be caused by the increased systematic difference between the coupled model and the analysis that uses observed SSTs. The ensemble spread is not changed significantly due to the coupling from initial time (not shown).

Additional insight into the geographical distribution of the impact can be obtained by studying maps of the change of the ensemble mean rms error. The improvement in the SST is mirrored in the temperature at 1000 hPa. In the tropics, coupling leads to a reduced rms error in the late medium-range (day 6 to 10), which is most pronounced over the Maritime continent. The winds in the lower troposphere improve over

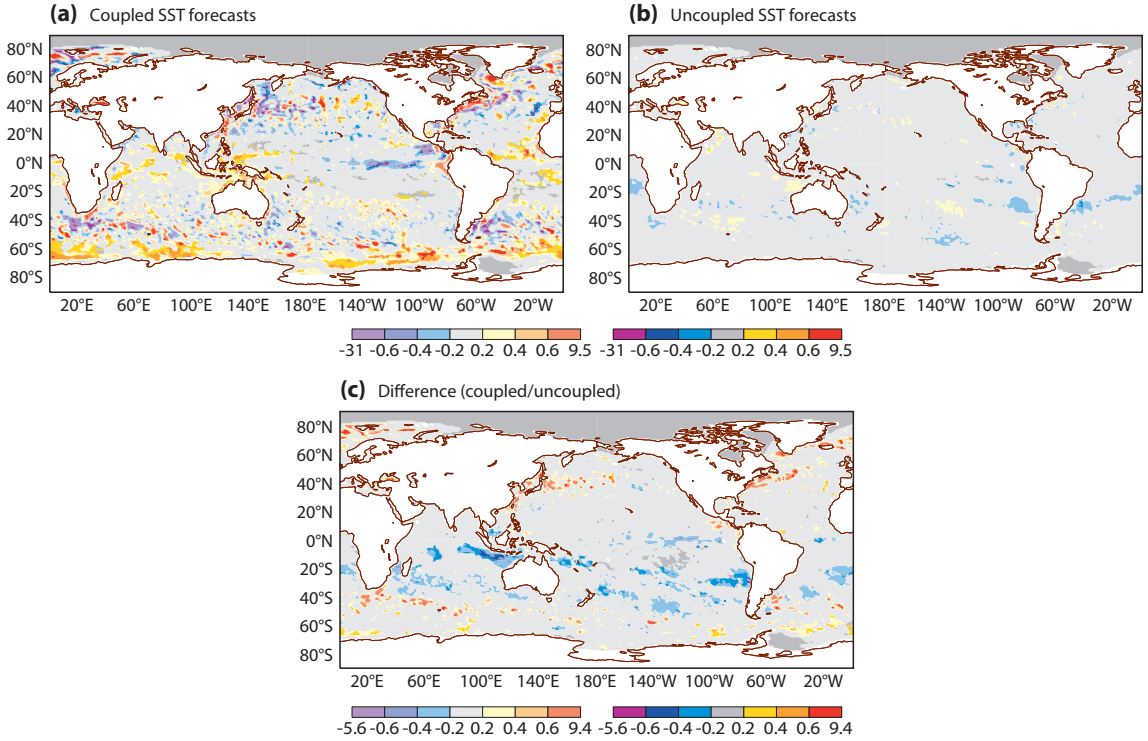

Figure 14: Mean error of 10-day ensemble mean forecast for (a) coupled and (b) uncoupled SST forecasts as well as (c) difference (coupled−uncoupled) in mean absolute error of day-10 ensemble mean forecasts. 33 cases in January–March 2012. Bold colours indicate statistical significance at the 95% level.

the Indian Ocean while the upper tropospheric winds improve more globally. Finally, there is a distinct reduction in error evident around 200 hPa east of the Himalayas for both temperature and zonal winds, but this change needs more diagnostics to understand the mechanisms behind and possible relations to the improvements over Indian Ocean and the Maritime continent.

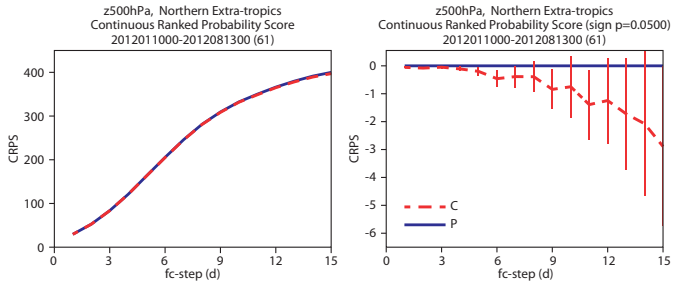

Figure 15: Impact of coupling with the ocean model from initial time on the continuous ranked probability score (CRPS) of 500 hPa geopotential in the northern extratropics (20N–90N). Panel (a) shows the CRPS of experiments $\mathscr{C}$ and $\mathscr{P}$ while (b) shows the CRPS difference between $\mathscr{C}$ and $\mathscr{P}$ with confidence intervals indicating the 95% probability level. Combined sample of 61 cases.

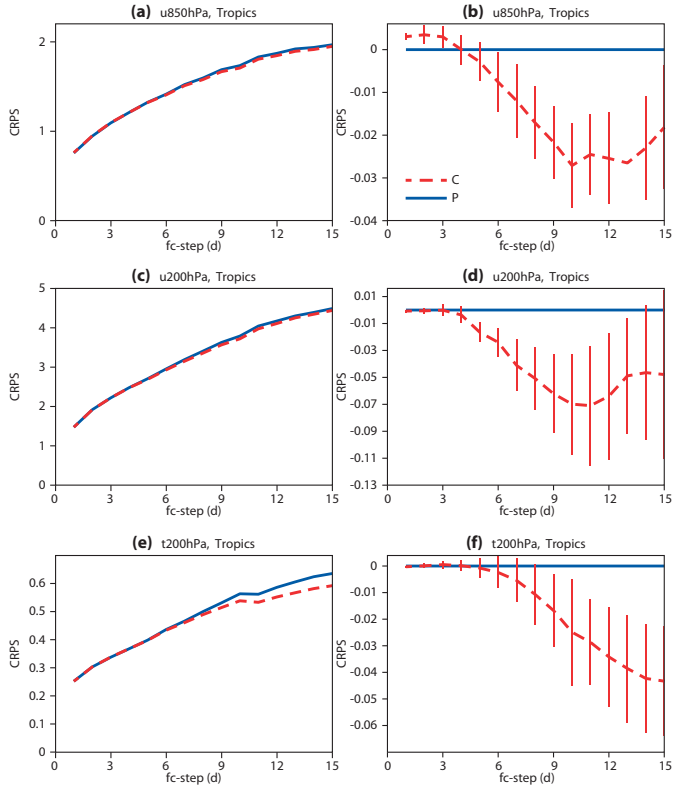

Figure 16: As previous figure but for the tropics and (a,b) zonal wind at 850 hPa, (c,d) zonal wind at 200 hPa and (e,f) temperature at 200 hPa.

6 Conclusions

In this paper an overview has been presented of the role ocean waves play in air-sea interaction, in particular for upper-ocean mixing and dynamics. We have studied the impact of sea-state dependent forcing, the Stokes-Coriolis force and the enhanced mixing by breaking ocean waves on the mean SST fields from NEMO in forced mode and in fully coupled integrations with the IFS-WAM-NEMO model. It is concluded that the sea-state dependent mixing is the main contributor to the impact on the ocean. Errors in SST obtained from standalone runs and from coupled simulations on the seasonal timescale show a certain degree of similarity. In the Summertime, in particular, the introduction of the sea-state dependent mixing gives a considerable improvement of the SST field and also of the seasonal cycle in, for example, the North Atlantic area. In addition, considerable improvements are found in the Kuro-Shio current and in the Gulfstream. Furthermore, impact on aspects of the ocean circulation such as the MOC were studied as well, but as far as we could see the sea-state dependent mixing did not influence the deep ocean.

It is, however, more difficult to assess whether sea state effects influence the skill of the seasonal forecasting system. At the moment there is weak evidence of improved skill in e.g. NINO3.4 and the North Atlantic area, but in other areas this is not so clear cut. However, as already pointed out in §4.2 the anomaly scores are obtained from SST's that have been corrected for the model drift, and therefore if the model drift is reduced this does not necessarily imply that there is improved skill. It is clear that more experimentation is required.

In the second part of this paper we have discussed possible benefits of coupling of the ocean and the

atmosphere from Day 0. Evidence has been presented that there are benefits for the prediction of hurricanes, for MJO prediction and there are also improvements in the skill of the ensemble prediction system, in particular in the tropics and to a lesser extent in the extra-tropics.

We conclude by pointing out that our work on the interaction of ocean waves and ocean circulation is still at its very beginning. Here, we have reported already some promising developments. Combined with the prospect of a sea-ice prediction capability and the prospect of a weakly coupled data assimilation system, very exciting times are indeed expected to lie ahead in the field of the interaction of ocean, atmosphere and ocean waves.

Acknowledgements. This work was partly supported by the European Union FP7 project MyWave (grant no 284455).

Appendix

A Supplementary Figures

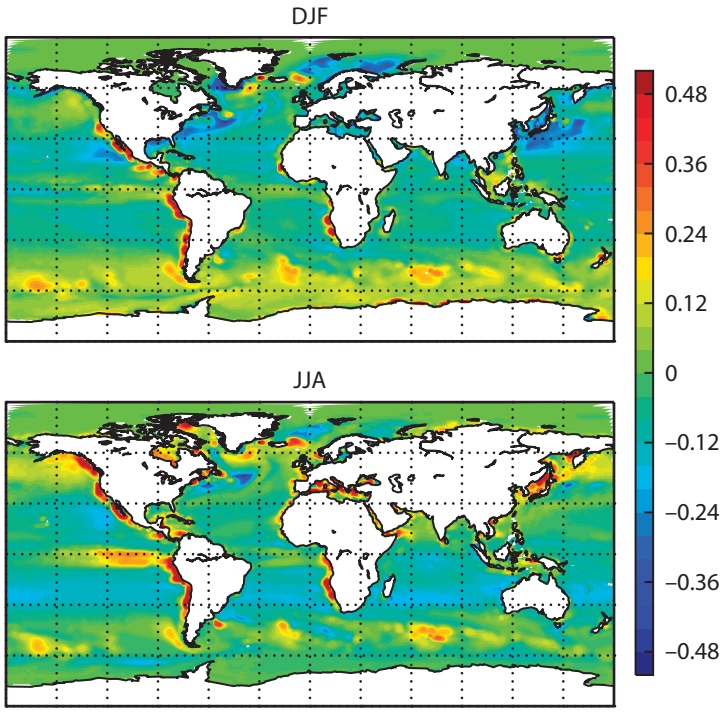

Figure A1: 20-yr average SST difference between CTRL (fsei) and a run with water-side stress from the ERA-Interim WAM model (TAUOC=fxdz).

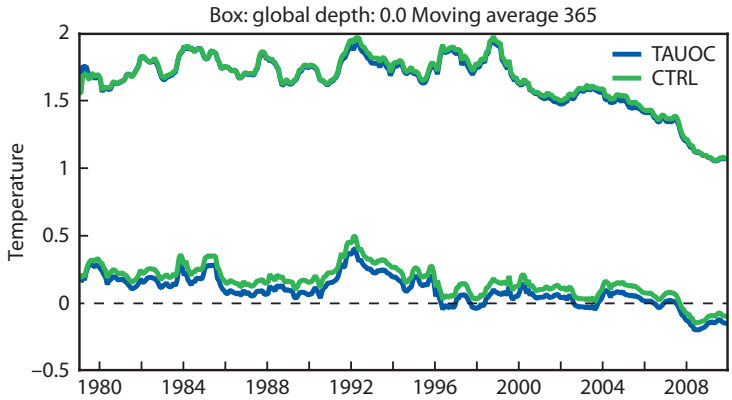

Figure A2: Time series of model bias (lower curves) and standard deviation (upper curves) for SST globally (CTRL=green, TAUOC=blue). A slight lowering of the bias is found. The trend is spurious and is the result of a substantial increase in observations over the model period.

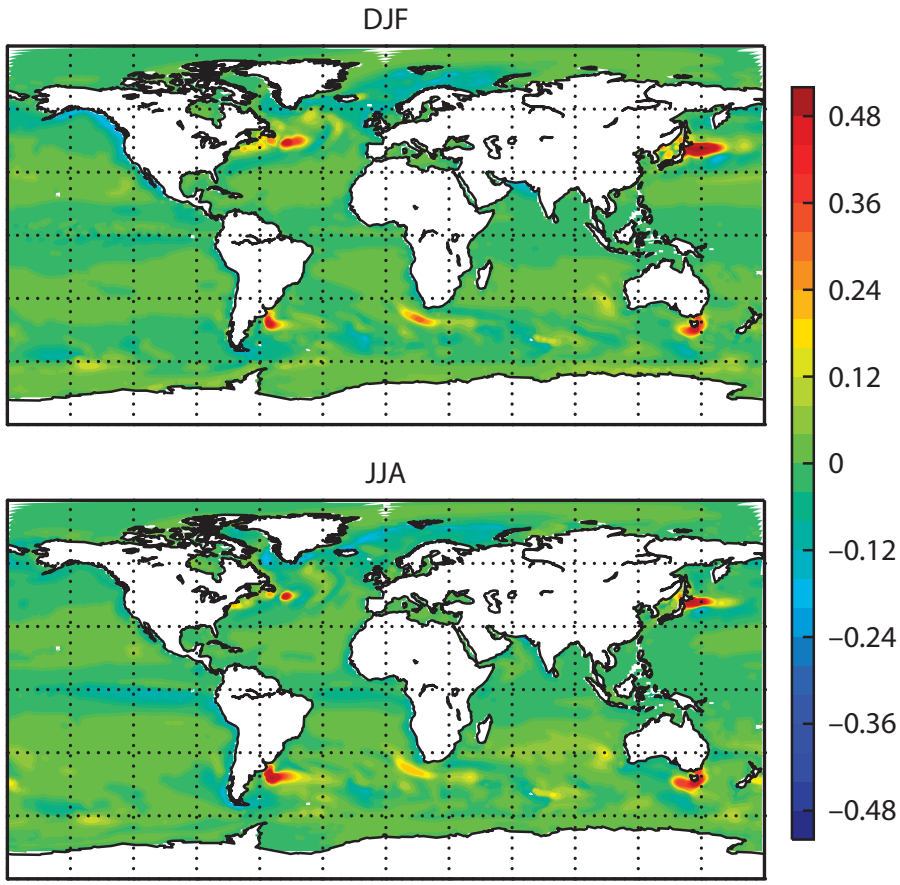

Figure A3: 20-yr average SST difference between CTRL (fsei) and a run with Stokes-Coriolis forcing as determined by the Stokes drift from the ERA-interim WAM model(STCOR=fsee). The differences are on the order of 0.5 K in the extratropics. The colour scale is ±0.5 K.

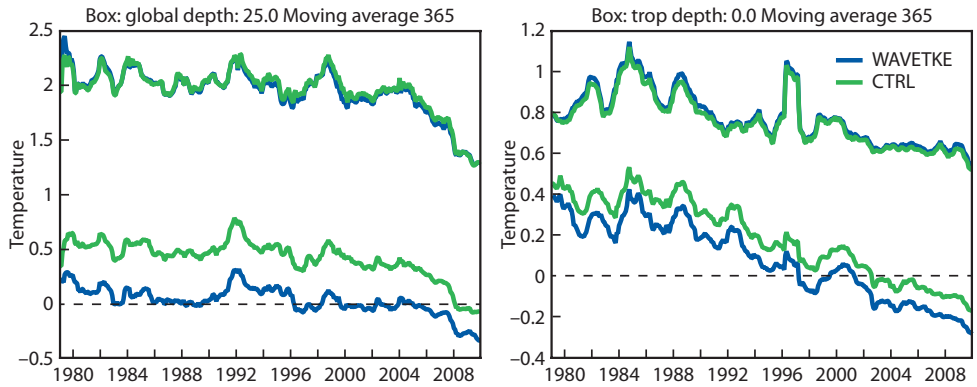

Figure A4: Panel a: Time series of model bias (lower curves) and standard deviation (upper curves) for observed temperature at 25 m depth globally (CTRL=green, TKEW=blue). Panel b: Same for surface temperature in the tropics. The trend is spurious and is the result of a substantial increase in observations over the model period. The bias at 25 m depth is greatly reduced most pronounced in the summer hemisphere, where the mixing is reduced, leading to higher SST.

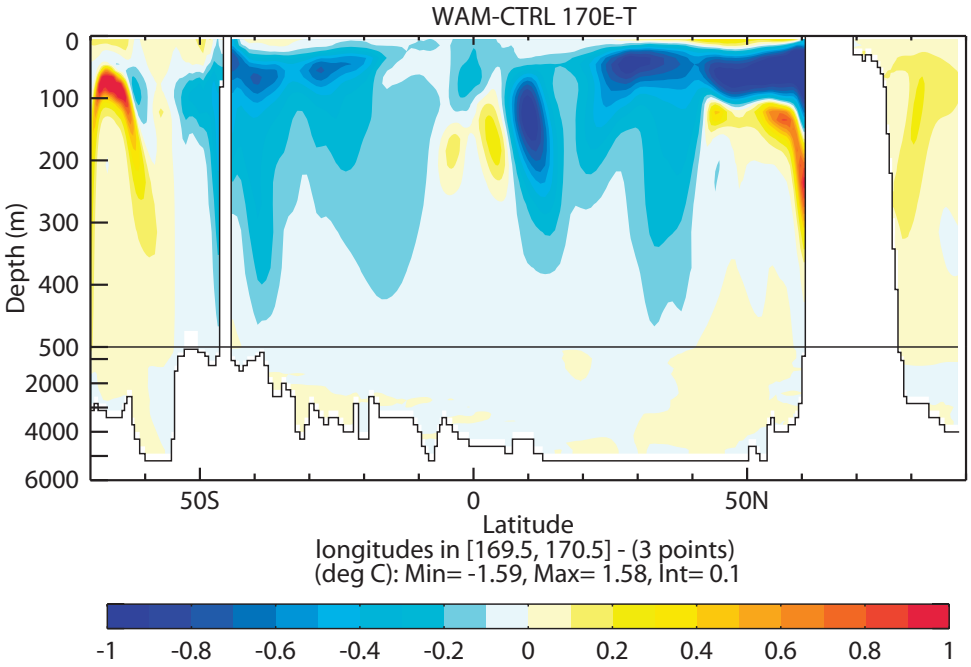

Figure A5: Panel a: Cross section at 170 E of the difference between temperature of WAM and CTRL. Impact of sea state dependent mixing is seen down to 400 m depth.

References

Abramowitz, M., Stegun, I. A. (Eds.), 1972. Handbook of Mathematical Functions, with Formulas, Graphs, and Mathematical Tables. Dover, New York.

Burchard, H., 2001. Simulating the Wave-Enhanced Layer under Breaking Surface Waves with Two-Equation Turbulence Models. *J. Phys. Oceanogr.* **31**, 3133-3145.

Craig, P.D. and M.L. Banner,1994. Modeling wave-enhanced turbulence in the ocean surface layer. *J. Phys. Oceanogr.* **24**, 2546-2559.

Dee, D.P., S. M. Uppala, A. J. Simmons, P. Berrisford, P. Poli, S. Kobayashi, U. Andrae, M. A. Balmaseda, G. Balsamo, P. Bauer, P. Bechtold, A. C. M. Beljaars, L. van de Berg, J. Bidlot, N. Bormann, C. Delsol, R. Dragani, M. Fuentes, A. J. Geer, L. Haimberger, S. B. Healy, H. Hersbach, E. V. Hólm, L. Isaksen, P. Kållberg, M. Köhler, M. Matricardi, A. P. McNally, B. M. Monge-Sanz, J.-J. Morcrette, B.-K. Park, C. Peubey, P. de Rosnay, C. Tavolato, J.-N. Thépaut, F. Vitart, 2011.The ERA-Interim reanalysis: configuration and performance of the data assimilation system. *Quart. J. Roy. Meteor. Soc.*,**137**, 553-597.

Edson, J., V. Jampana, R. Weller, S. Bigorre, A. Plueddemann, C. Fairall, S. Miller, L. Mahrt, D. Vickers, and H. Hersbach, 2013. On the exchange of Momentum over the open Ocean. *J. Phys. Oceanogr.*, doi:10.1175/JPO-D-12-0173.1, in press.

Gemmrich, J., 2010. Strong turbulence in the Wave Crest Region, *J. Phys. Oceanogr.* **40**, 583-595.

Gottschalk J., M. Wheeler, K. Weickmann, F. Vitart, N. Savage, H. Hendon, H. Lin, M. Flatau, D. Waliser, K. Sperber, W. Higgins and A. Vintzileos, 2009: Establishing and Assessing Operational Model

MJO Forecasts: A Project of the CLIVAR Madden-Julian Oscillation Working Group. *Bull. Am. Meteor. Soc.*, **91**, 1247-1258.

Grant A.L.M. and S.E. Belcher, 2009. Characteristics of Langmuir Turbulence in the Ocean Mixed layer, *J. Phys. Oceanogr.* **39**, 1871-1887.

Hasselmann, K., 1970. Wave-driven inertial oscillations. *Geophys. Fluid Dyn.* **1**, 463-502.

Hasselmann, K., 1971. On the mass and momentum transfer between short gravity waves and larger-scale motions. Part 1. *J. Fluid Mech.* **50**, 189-205.

Janssen, Peter, 2004. *The interaction of Ocean Waves and Wind*. Cambridge University Press, 308+viii pp.

Janssen, P., 2008. Air-sea interaction through waves. In: ECMWF Workshop on Ocean-Atmosphere Interactions, 10-12 November 2008. Available online at http://www.ecmwf.int/publications/. pp. 47–60.

Janssen, P.A.E.M., 2012. Ocean wave effects on the daily cycle in SST. *J. Geophys. Res.*, **117**, C00J32, 24 pp., doi:10.1029/2012JC007943.

Janssen, P.A.E.M. and P. Viterbo, 1996. Ocean Waves and the atmospheric Climate. *J. Climate* **9**, 1269-1287.

Janssen, P.A.E.M., J.D. Doyle, J. Bidlot, B. Hansen, L. Isaksen and P. Viterbo, 2002: Impact and feedback of ocean waves on the atmosphere. in *Advances in Fluid Mechanics*, **33**, Atmosphere-Ocean Interactions ,Vol. I, Ed. W.Perrie.

Janssen, P.A.E.M., O. Saetra, C. Wettre, H. Hersbach and J. Bidlot, 2004. Impact of the sea state on the atmosphere and ocean. Annales Hydrographiques 6e série, **3** (772), 3,1,3,23.

Jenkins, A.D., 1987a. A lagrangian model for wind- and wave-induced near-surface currents. *Coastal Engineering* **11**, 513-526.

Komen, G.J., L. Cavaleri, M. Donelan, K. Hasselmann, S. Hasselmann, and P.A.E.M. Janssen, 1994: *Dynamics and Modelling of Ocean waves* (Cambridge University Press, Cambridge)

Longuet-Higgins, M.S. and R.W. Stewart, 1961. The changes in amplitude of short gravity waves on steady non-uniform currents. *J. Fluid Mech.* **10**, 529-549.

Magnusson, L., M. Alonso-Balmaseda, F. Molteni, 2012. On the dependence of ENSO simulation on the coupled model mean state. *Clim. Dyn.*, doi: 10.1007/s00382-012-1574-y

Mastenbroek, C., G.J.H. Burgers and P.A.E.M. Janssen, 1993. The dynamical coupling of a wave model and a storm surge model through the atmospheric boundary layer. *J. Phys. Oceanogr.* **23**, 1856-1866.

McWilliams, J.C., and J.M. Restrepo, 1999. The wave-driven ocean circulation. *J. Phys. Oceanogr.* **29**, 2523-2540.

Mellor, G.L. and A. Blumberg, 2004. Wave breaking and Ocean Surface Layer Thermal Response. *J. Phys. Oceanogr.* **34**, 693-698.

Mellor, G.L. and T. Yamada, 1982. Development of a turbulence closure model for geophysical fluid problems. *Rev. Geophys. Space Phys.* **20**, 851-875.

Mogensen, K., S. Keeley and P. Towers, Coupling of the NEMO and IFS models in a single executable, ECMWF Technical Memorandum No 673, 2012.

Moon, I., I. Ginis, T. Hara, and B. Thomas, 2007: Physics-based parameterization of air-sea momentum at high wind speeds and its impact on hurricane intensity predictions. *Mon. Wea. Rev.*, **135**, 2869-2878.

Phillips, O.M., 1977. The dynamics of the upper ocean, Cambridge University Press, Cambridge, 336p.

Rascle, N., Ardhuin, F. and E. Terray, 2006. Drift and mixing under the ocean surface: A coherent one-dimensional description with application to unstratified conditions. J Geophys Res 111 (C3), C03016, 16pp, doi:10.1029/2005JC003004.

Reynolds RW, Rayner NA, Smith TM, C SD, Wang W. 2002. An improved in situ and satellite SST analysis for climate. *J. Climate.***15**, 1609â1625.

Saetra, Ø., Albretsen, J. and P. Janssen, 2007. Sea-State-Dependent Momentum Fluxes for Ocean Modeling. J Phys Oceanogr 37 (11), 2714–2725, doi:10.1175/2007JPO3582.1.

Shay, L.K., G.J. Ginis and P.G. Black, 2000: Effects of a warm oceanic feature on hurricane Opal. *Mon. Wea. Rev.* **125(5)**, 1366-1383.

Shay, L.K., and W. Uhlhorn, 2008: Loop Current response to hurricanes isodore and Lili. *Mon. Wea. Rev.*, **136**, 3248-3274.

Terray, E.A., M.A. Donelan, Y.C. Agrawal, W.M. Drennan, K.K. Kahma, A.J. Williams, P.A. Hwang and S.A. Kitaigorodskii, 1996. Estimates of Kinetic Energy Dissipation under Breaking Waves. *J. Phys. Oceanogr.* **26**, 792-807.

Wheeler, M.C. and H.H. Hendon, 2004: An all-season real-time multivariate MJO index: Development of an index for monitoring and prediction. *Mon. Wea. Rev.*, **132**, 1917-1932.

Whitham, G.B. (1962). Mass, momentum and energy flux in water waves. *J. Fluid Mech.* **12**, 135-147.

Whitham, G.B., 1974. *Linear and nonlinear waves*, Wiley, New York, 636p.

Woolnough, S. J., F. Vitart and M. A, Balmaseda, 2007: The role of the ocean in the Madden-Julian Oscillation: Implications for MJO prediction. *Quart. J. Roy. Meteor. Soc.*, **133**, 117-128.

Yablonski. R.M. and I. Ginis, 2008: Improving the initialization of coupled hurricane-ocean models by assimilating mesoscale oceanic features. *Mon. Wea. Rev.*, **136**, 2592-2607.